PERGAMON

Progress in Surface Science 61 (1999) 23–84

Progress in SURFACE SCIENCE

www.elsevier.com/locate/progsurf

Review Article

Interaction of slow, very highly charged ions with surfaces

T. Schenkel*, A.V. Hamza, A.V. Barnes, D.H. Schneider

University of California, Lawrence Livermore National Laboratory, Livermore, CA 94551, USA

Abstract

The present article reviews recent advances in the studies of the interaction of slow ($v < v_{\mathrm{Bohr}}$), very highly charged ions (such as Xe^{52+} and Au^{69+}) with surfaces of metals, semiconductors, and insulators (including biological materials). After a brief summary of past developments, we describe key experimental techniques for studies of secondary particle emission and the de-excitation dynamics of the highly charged ions. Recent progress in measurement and determination of the mechanisms leading to secondary electron yields, secondary ion yields and total sputtering yields will be discussed. The de-excitation dynamics are addressed in experiments on projectile neutralization and energy loss in thin films of material. We review the theoretical concepts briefly and introduce theoretical models in the discussion of experimental results. Following the presentation of fundamental studies we will address emerging applications of slow, very highly charged ions in surface analysis and surface modification. © 1999 Published by Elsevier Science Ltd. All rights reserved.

Contents

1. Historical overview 25
    1.1. Phenomena occurring in SHCI-surface interactions 26
    1.2. Highly charged ion sources 27

---

* Corresponding author.
E-mail address: schenkel2@llnl.gov (T. Schenkel)

0079-6816/99/$ - see front matter © 1999 Published by Elsevier Science Ltd. All rights reserved.
PII: S0079-6816(99)00009-X

Nomenclature

AFM	Atomic Force Microscopy
COB	Classical-Over-The Barrier
DIET	Desorption Induced by Electronic Transitions
EBIS	Electron Beam Ion Source
EBIT	Electron Beam Ion Trap
ECR	Electron Cyclotron Resonance
ERD	Elastic Recoil Detection
HCI	Highly Charged Ions
IDE	Internal Dielectronic Excitation
HIBS	Heavy Ion Backscattering
OBM	Over-Barrier Model
PMMA	Polymethylmethacrylate
PIPS	Particle Implanted and Passivated Silicon
SAM	Self-Assembled Monolayers
SHCI	Slow, Highly Charged Ions
SIMS	Secondary Ion Mass Spectroscopy
SRIM	Stopping and Range of Ions in Matter
STE	Self Trapped Excitons
STH	Self Trapped Holes
TAC	Time-to-Amplitude Converter
TOF	Time-of-Flight

2. Experimental techniques 28
  2.1. Electrostatic charge state analysis and transmission energy loss measurements 28
  2.2. Electron counting 29
  2.3. Sputter yield measurements via microbalance technique 30
  2.4. Sputter yield measurements via catcher surface technique 31
  2.5. Time-of-flight secondary ion mass spectrometry with highly charged projectiles 33
  2.6. Ion implanted silicon detectors 33
  2.7. X-ray detection techniques 34
    2.7.1. Solid state detectors 34
    2.7.2. Crystal spectrometers 35
    2.7.3. Calorimetric spectrometers 35

3. Experimental results 35
  3.1. Charge equilibration time of SHCI in solids 35
  3.2. Charge state dependent energy loss 39
  3.3. Electron emission 42
  3.4. X-ray emission studies 47
    3.4.1. K-shell X-ray emission 49

3.4.2. L-shell X-ray emission 55
3.4.3. M-shell X-ray emission 58
3.4.4. Soft X-ray emission studies 60
3.5. Sputtering of surface atoms 62
3.5.1. Total sputter yields 63
3.5.2. Secondary ion emission 63
3.6. Deposition of potential energy in solids 69

4. Theoretical models of sputtering by SHCI 69
4.1. Defect mediated desorption 69
4.2. Coulomb explosion sputtering 70
4.3. Sputtering by intense, ultrafast electronic excitations 71
4.4. Microscopic mechanisms for sputtering by SHCI: conclusions 72

5. Emerging applications 73
5.1. Highly charged ion based secondary ion mass spectrometry 73
5.1.1. Coincidence counting 75
5.2. Emission microscopy 76
5.3. SHCI driven X-ray source 76
5.4. Surface modification 77

Acknowledgements 79

References 79

---

1. Historical overview

Excellent reviews of the slow, multiply charged ions-surface interactions were given by Arnau et al. [1] and Schneider and Briere [2] covering the state of the field through 1995. Due to the rapid developments in this area in the last three years, it is valuable to review the progress in this time frame. Therefore, this review concentrates on experimental progress from 1995 through 1998 and discusses theoretical models and progress in context of the experimental evidence.

For the purposes of this review, we consider 'surfaces' to be solid and to consist of the vacuum–solid interface and the adjacent surface and subsurface layers. In some cases we include up to 50 atomic layers in our discussion. We deal with *slow, highly charged ions* (SHCI). Slow is defined as velocities less than the Bohr velocity ($v_{\mathrm{Bohr}} = v_0 = 2.19 \times 10^6$ m/s). Thus, the motion of electrons is fast compared to the nuclear motion of the system and the projectiles will interact with the surface initially very far from their charge state 'equilibrium'. Key questions that research in this field is striving to answer is how does the solid surface respond to transfer of the potential energy of the SHCI and what are the applications of the surface response. The potential energy of a SHCI is the sum of ionization potentials of the ion. For example Xe^{54+} has ~202 keV of potential energy. In most of the discussion in this review the potential energy deposition of the SHCI has a much greater effect on the surface than the kinetic energy deposition of the SHCI.

1.1. Phenomena occurring in SHCI-surface interactions

The current views of the interaction of SHCI with surfaces are not in complete agreement. As a starting point for our discussion we will describe one current picture of the SHCI-surface interaction.

As the SHCI approaches a surface, the SHCI induces a collective response of the surface electrons, creating an 'image charge'. The image charge accelerates the SHCI towards the surface and, thus, sets a lower limit to the ion velocity. Neutralization of the slow SHCI begins above surfaces and can be described by a 'classical-over-the-barrier' model for ion-surface interactions [3]. The image interaction also affects the height of the 'barrier' and the electronic states of the projectile. When the SHCI reaches a critical distance above the surface, electrons from the surface are resonantly captured into high-lying, quasi-stationary Rydberg states. The capture into these Rydberg states should continue until the SHCI is essentially neutral. This is the formation of a 'hollow' atom, the initially present inner shell vacancies are still present. The hollow atom will shrink by rapid autoionization, but it will be kept neutral by ongoing resonant capture into high-lying Rydberg states. Tighter bound projectile states will be populated as they come into resonance with surface states as the SHCI moves closer to the surface and due to the above mentioned autoionization processes. In addition as the occupied Rydberg projectile states come into resonance with empty surface states due to closer approach to the surface, electrons will be recaptured by the surface. The resulting above-surface neutralization picture is a constantly shrinking electron cloud around the originally highly charged ion.

At close contact with the surface, screening by the surface electrons will 'peel off' the outer electrons of the not yet relaxed SHCI. A second, more compact, hollow atom will be formed below the surface. The electrons of the solid will form a compact screening cloud around the SHCI with states of lower principal quantum number. The formation time of the cloud will be related to the plasmon frequency of the material. Below the surface the hollow atom may de-excite by three mechanisms. First, Auger neutralization can fill the inner shell vacancies; second, close collision with target atoms can fill vacancies via quasi-molecular transitions, ('side-feeding') and, third, inner shell vacancies can decay via characteristic X-ray emission. The above- and below-surface Auger processes and the peel off process account for the emission of electrons during the interaction.

Only a small fraction of the initial potential energy carried by the SHCI can be accounted for in the emitted secondary electrons (~1%) and X-rays (~5%). Since the SHCI neutralizes in a few femtoseconds (see Section 3.1) and surface atomic motion requires time scales of picoseconds, the major portion of the potential energy is initially deposited into the electronic system of the surface. The electronic excitation of the surface and near-surface region is sustained on the order of picoseconds in order to transfer energy to the lattice as evidenced by the sputtering of neutral atoms and clusters and secondary ions from the surface.

1.2. Highly charged ion sources

Recent experimental advances in the interaction of SHCI with surfaces have benefited to a large extent from the advances in ion source technology. The mainstay sources in this field have traditionally been the *electron cyclotron resonance* (ECR) ion source, the *electron beam ion source* (EBIS) and the *electron beam ion trap* (EBIT) ion source. These sources can produce highly charged ions at low velocity such that these ions are very far from charge state equilibrium. Each of these sources has been described previously [1,2]. In this section only the advances since 1996 will be discussed.

Xie and Lyneis [4], Xie [5], and Alton et al. [6] report on enhancing the performance of traditional electron cyclotron resonance ion sources with multiple-discrete-frequency microwave radiation. The creation of a large ECR plasma 'volume' permits coupling of more power into the plasma, resulting in heating a much larger electron population to much higher energies. The heating produces higher charge state distributions and higher intensities within a particular charge state. The ECR plasma 'volume' can be increased by injecting broadband or multiple-discrete frequency microwave radiation. Xie [5] has shown that combining the multiple frequency heating with Al_2O_3 surface coatings (additional source of cold electrons) and higher magnetic mirror fields (to improve plasma confinement) has produced the highest charge state ion beams from ECR ion sources.

Nakagawa et al. [7] have demonstrated the production of highly charged heavy ions in an ECR ion source (RIKEN 18 GHz ECRIS) by injection of organometallic compounds.

Metalocenes were used to inject Fe, Ni, Ru and Os, and hexacarbonyls were used to inject Cr, Mo, and W into the plasma. The metalocenes produced an order of magnitude higher beam current (100 eμA) than the hexacarbonyls. The authors suggest the weaker bonding of the metalocene is responsible for the higher currents. Numerical simulation of the ECR plasma may lead to improved operating parameters as well [8].

The extraction system for EBIT sources [2] has been improved by increasing the radius of bender elements. Ratliff et al. [9] and Schenkel et al. [10] have both measured extracted ion fluxes for Xe^{44+} of $\sim 3 \times 10^6$ ions/s from their EBIT sources after beamline upgrades. The higher fluxes have allowed greater flexibility in experimental measurements. In addition extraction of highly charged ions up to U^{90+} from the 'Super-EBIT' has been demonstrated [11].

In two papers Stöckli et al. [12] and Stöckli [13] have described techniques for varying the time structure from continuous to pulsed, including 'microbunched,' highly charged ion beams from the Kansas State University EBIS. These techniques allow users to select the characteristics most desirable for their experiments (e.g., high peak intensity or high average flux). Microbunching is a repetitive partial lowering of the last drift tube potential to allow the hottest ions to escape. The peak intensity of the micro-pulse (100 μs duration) at 4.5 kHz or 80 microbunches is twice the peak intensity of the slow expulsion mode. The peak intensity at 415 Hz or 6–8 microbunches is 20 times the slow expulsion mode intensity.

Demyanov et al. [14] have designed a laser ion source to produce highly charged ions. The ion extraction is performed by spherical grid electrodes, which increase the extraction efficiency several hundred fold.

2. Experimental techniques

2.1. Electrostatic charge state analysis and transmission energy loss measurements

Following transmission through thin foil targets, projectiles can be separated in the field of two parallel plates according to their charge state (Fig. 1). Charge-separated beams are then detected with a position-sensitive microchannel plate detector. Different positions on the detector correspond to different charge states of transmitted projectiles.

The detector can be moved in the direction of charge-state-analysis so that charge states up to about 30+ are accessible for a detector with an effective

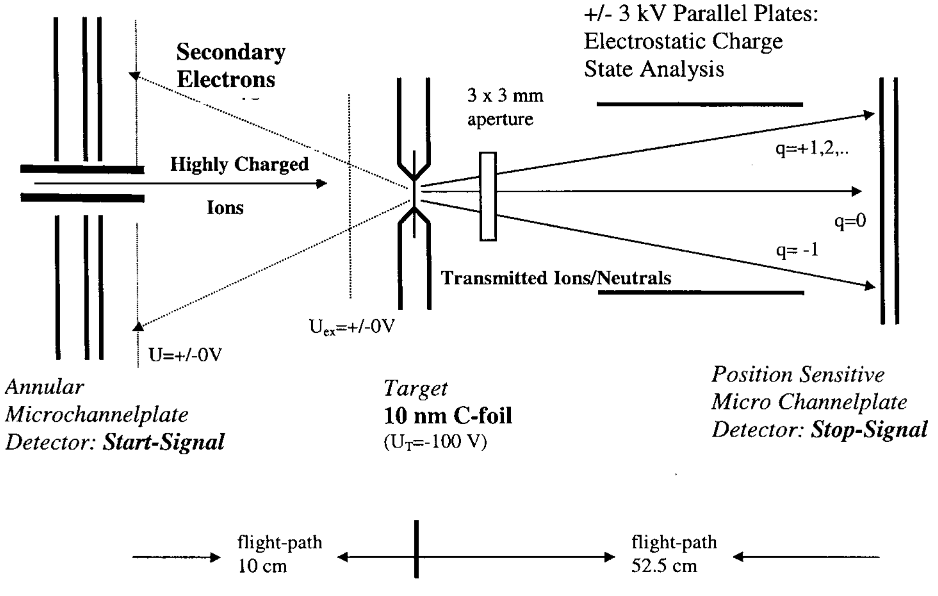
+/- 3 kV Parallel Plates:
Electrostatic Charge
State Analysis
Secondary
Electrons
3 x 3 mm
aperture
Highly Charged
Ions
q=+1,2,..
q=0
q= -1
Transmitted Ions/Neutrals
U=+/-0V
U_{ex}=+/-0V
Annular
Microchannelplate
Detector: Start-Signal
Target
10 nm C-foil
(U_T=-100 V)
Position Sensitive
Micro Channelplate
Detector: Stop-Signal
flight-path
10 cm
flight-path
52.5 cm

Fig. 1. Schematic of the experiment setup for charge-state-analysis and transmission energy loss measurements [15,19,164].

diameter of 4.5 cm. Signal to noise ratios in these measurements can be improved significantly by requiring coincident electron emission following impact of an SHCI on the foil target and detection of a transmitted projectile. Using the pulse of low energy secondary electrons to start and the transmitted ions as a stop trigger of a timing device (e.g., a *time-to-amplitude converter*, or TAC) provides a measurement of the flight time of ions from the foil surface to the stop-detector. Given that incident velocity and flight path are known, this flight time allows for a determination of the energy loss of SHCI in the foil target.

Practical lower limits for foil thickness are about 5 nm (~1 μg/cm^2) for carbon foils. Layers of other materials can be deposited on thin carbon foils by, for example, evaporation [15].

Combining charge-state-analysis and energy loss measurements, it is further possible to investigate correlations of exit charge states with energy loss values in an event-by-event analysis. So far, such correlations have been observed, but they have been only minor effects (see Section 3.2 [16]).

The energy of charged projectiles after transmission through foil targets or after grazing incidence scattering can also be determined with, for example, hemispherical electrostatic analyzers [17,18].

2.2. Electron counting

Traditionally there have been two methods to determine the electron emission from surfaces after SHCI impact [1]. Briefly, the first is the current method. This involves measuring the target current with and without permitting electrons to leave the sample via appropriate biasing of the target. Precautions have to be taken to account for secondary ion emission and spurious electron emission from scattered or reflected particles. For the current measurement, typically, ion beam fluxes greater than 1 nA are required.

The second method measures the electron emission statistics. In this method, electrons emitted with less than 60 eV are deflected by a conical electrode and, then, after extraction, are focused onto a surface barrier detector biased at +20 kV with respect to the target. Since the detector electronics can not distinguish individual electrons from one highly charged ion impact, the electrons from one impact will be registered as one electron with n times 20 keV energy. Thus, the area below the nth peak in the energy spectrum is directly related to the probability of the emission of n electrons. The first moment of the probability distribution gives the electron yield. Primary SHCI fluxes of less than 10^3 ions/s are required to perform the electron emission statistics measurement.

Eder et al. [20] have improved their electron emission statistics method by adding an acceleration/deceleration lens to vary the kinetic energy of the primary SHCI beam from nominal zero to 40 keV/q kinetic energy. The advance affords a rather straightforward way of separating potential electron emission (due to the potential energy carried by the ion) from kinetic electron emission (due to the kinetic energy carried by the ion) from projectiles incident along the surface normal. Using this technique for multiply charged oxygen and nitrogen ions impinging on a polycrystalline gold target, Eder et al. [20] showed that for differently charged ion species, a difference in electron yield due to charge-related potential energy is almost independent of the projectile impact energy.

Lemell et al. [21] have further developed an approach to separate potential electron emission from kinetic electron emission in grazing incidence. In this technique the electron emission statistics are correlated with specific projectile trajectories characterized by the resulting scattering angle. A comparison to electron emission data for normal incidence with the same projectile, charge state, target and velocity normal to the surface allows direct identification of potential and kinetic electron emission near the kinetic electron emission threshold.

Relative electron emission from surfaces as a function of projectile charge and incident kinetic energy can be measured with a microchannel plate detector. Schenkel et al. [19,164] used an annular microchannel plate detector to determine relative electron yield with pulse height analysis from metal and insulator surfaces. The target surfaces were biased at -2 kV to allow for efficient secondary electron detection. While kinetic and potential electron emission cannot be separated in these measurements, the relative electron yield is measured in a regime where the kinetic electron emission is fairly independent of incident kinetic energy. The relative yield could be calibrated by previous measurements of the total electron yield from gold surfaces [22].

For energy analysis of emitted electrons various types of electrostatic spectrometers are used [1]. The technology for energy analysis of electrons is relatively advanced and, for the most part, commercially available. The reader is directed to other sources for a detailed description [23].

2.3. Sputter yield measurements via microbalance technique

The determination of sputter yields for impact of highly charged ions on surface is relatively difficult because of the limited flux produced by SHCI sources. Neidhart et al. [24,165] and Sporn et al. [25] have improved the sensitivity of quartz crystal microbalance techniques to determine sputter yields for SHCI impacts. The ion bombardment causes an increase of the crystal's resonance frequency, which is a direct measure of the mass loss. The frequency stability and, thus, sensitivity, are improved by using the planoconvex SC-cut quartz crystals, one side of which is coated with a thin film of the polycrystalline material to be sputtered. The resonance frequency is further stabilized by operating the quartz crystals within 0.1°C of the minimum of their frequency versus temperature curve (150°C). The sensitivity limit for the optimized microbalance technique is 10^{-3} monolayers or about 10^{12} atoms removed per s. In addition, the SC-cut crystals have a resonance frequency insensitive to radial stress. This technique does not require knowledge of the collection geometry and the neutral particle sticking coefficient (see catcher techniques), and also does not allow measurement on single crystal surfaces or macroscopically thick samples.

2.4. Sputter yield measurements via catcher surface technique

Yields of sputtered material have traditionally been determined with a variety of techniques such as weight loss measurements and crater profiling. However, low SHCI beam intensities of about 10^5–10^6 ions per s for Th^{70+} and Xe^{44+} set high demands on detection sensitivity. At a sputter yield of 100 atoms removed per incident projectile and a sensitivity limit of 10^{-3} monolayer, the microbalance technique can be used with beam currents down to a few nA or 10^{10} projectiles per s. Sputter yields from a variety of materials have been determined for SHCI up to Xe^{27+} with the microbalance technique (see Section 2.3).

Alternatively, collection of ablated material on a catcher surface (Fig. 2) allows for determination of sputter yields from surface coverages of accumulated material. Sensitivities of about 10^{13} atoms per cm^2 have been achieved by Rutherford backscattering analysis with MeV heavy ion beams [26]. In a recent development, Banks and co-workers have optimized the sensitivity for analysis of impurities on silicon wafers using 100 keV carbon beams in a time-of-flight *heavy ion backscattering scheme* (HIBS). Here, it is possible to quantify heavy metal coverages as low as 10^9 atoms/cm^2 on otherwise clean silicon [27].

The coverage of ablated atoms of material A on the catcher, $\theta(A)$, is given by the following relation [28]:

$$\theta(A) = Dsc(A)\Omega(\vartheta)S(\varphi) \tag{1}$$

Here, D is the SHCI dose and $S(\varphi)$ is the sputter yield (i.e. atoms removed per SHCI). The sputter yield depends on the incident angle of the SHCI, φ. The

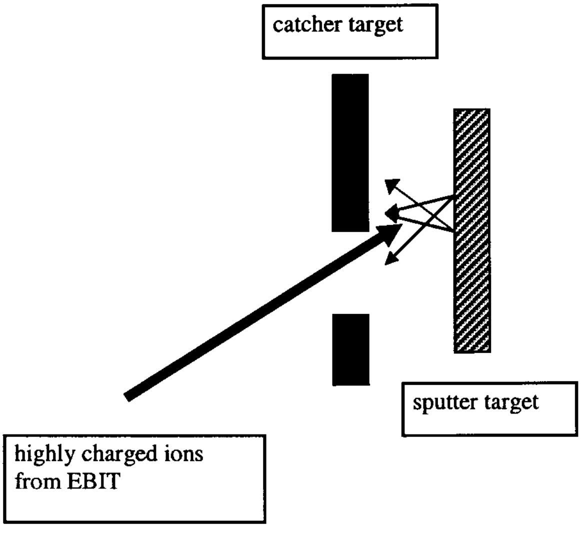

Fig. 2. Geometry for collection of sputtered material on a catcher surface.

sticking coefficient, s, gives the probability that an emitted particle sticks to the catcher surface. Sticking coefficients have been quantified only for a few catcher systems and have been found to be close to unity [26]. $c(A)$ is the relative concentration of A on the surface of the sputter target. The view factor, $\Omega(\upsilon)$, of the catcher surface for emitted particles from the sputter target is determined by the distance between the two, by the angular distribution of emitted secondaries, the beam spot size and the size of the exposed area on the catcher surface [28,29]. The dependency of SHCI induced sputtering on the incident angle is not known, and neither is the angular distribution of emitted secondaries. In the simplest approximation, the latter is assumed to be cosine.

Using the catcher technique with subsequent HIBS analysis it was possible to measure sputter yields for gallium arsenide and uranium oxide interacting with SHCI up to Th^{70+} [10,30]. Relative uncertainties of the resulting sputter yields are dominated by variations in view factors between consecutive measurements, by uncertainties in SHCI dose, and by uncertainties in HIBS results. The combined relative uncertainty can be smaller than 20%. Absolute uncertainties result mostly from assumptions of unknown angular distributions in the calculation of the view

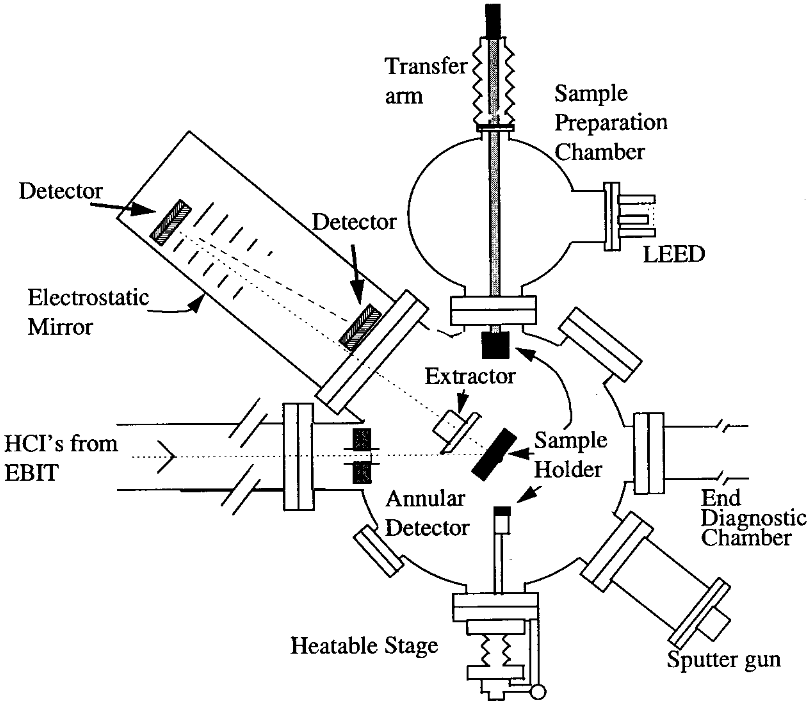
Transfer arm
Sample Preparation Chamber
Detector
Detector
LEED
Electrostatic Mirror
Extractor
HCI's from EBIT
Sample Holder
Annular Detector
End Diagnostic Chamber
Heatable Stage
Sputter gun

Fig. 3. Schematic of time-of-flight secondary ion mass spectrometry setup with annular detector and reflectron [34].

factor. A conservative estimate of uncertainties in total sputter yields determined by the catcher technique is about 50% [10].

2.5. Time-of-flight secondary ion mass spectrometry with highly charged projectiles

SHCI induce emission of a large ($>q$) number of mostly low energy (<20 eV) secondary electrons when they interact with surfaces. This pulse of electrons can be used as a start trigger of a multi-stop timing analyzer (e.g. ORTEC PTA 9308). Negative secondary ions are accelerated by the selected target bias and reach the detector after a characteristic flight time. The latter is proportional to the flight path and the square root of the ratio of accelerating voltage and secondary ion mass; for more details see reference [31]. *Time-of-flight secondary ion mass spectrometry* (TOF-SIMS) is a standard surface analysis technique [32]. Projectiles are bunched into groups of a few hundred primary ions and bunch widths are typically <1 ns. In the scheme for SHCI, time-of-flight cycles are started by individual projectiles. Copious electron emission affords a start efficiency near 100% in negative polarity for SHCI with $q>20+$. In positive polarity, TOF cycles can be started by protons instead of electrons. Here, the start efficiency is typically $>50\%$ for $q>40+$. In the special case of thin foil targets, transmitted projectiles can also be used as start triggers in both polarities. While the mass resolution in this configuration is compromised by energy loss straggling in the foils, these measurements allow for an important cross-check. Spectra accumulated by starting time-of-flight cycles either on transmitted ions or on secondary electrons or protons have been found to exhibit identical structures [33]. The perturbation induced by SHCI is sufficiently strong to avoid distortions in spectra of secondary ions when requiring coincidences with secondary electrons or protons. A typical setup of a scattering chamber with TOF-SIMS capability is shown in Fig. 3. Secondary ions can be detected either in an annular microchannel plate detector after a flight path of only 10 cm or after reflection in an electrostatic mirror and a flight path of about 2 m. The mass resolution, $m/\Delta m$, achieved to date is about 2000 at mass 28 μ. Optimization towards resolutions around 10,000, as they are state of the art with singly charged ions TOF-SIMS, is in progress. The mass resolution of the short linear setup is only about 50 at mass 28 μ.

Typical SHCI beam currents for TOF-SIMS studies range from 10^3 to 10^4 ion per s. These very low ion currents make TOF-SIMS very favorable for use with SHCI. In comparison, quadruple or magnetic sector mass spectrometry schemes [32] require beam currents in the nA range. Also, single ion triggering enables event-by-event analysis of coincidences among secondary ions that were emitted by a single SHCI see Section 5.1.

2.6. Ion implanted silicon detectors

(PIPS) *Particle implanted and passivated silicon detectors* [35] were developed from surface barrier detectors by substituting the metal front contact with a thin (about 50 nm thick) layer of ion implanted silicon. The doped layer has a high concentration of boron and is passivated with a few nm of SiO_2. Due to the very thin insensitive contact layer, the energy resolution of PIPS in spectroscopy of fast, light ions is approaching the physical limit. The use of PIPS for spectroscopy of slow, highly charged ions is at first questionable. Since SHCI have velocities below the Bohr-velocity, nuclear stopping exceeds electronic stopping for heavy SHCI species and this translates into significant pulse height defects [35]. The signal from PIPS detectors is a pulse of collected charge from electron-hole pairs, created in the depletion region of the detector by energetic particles such as ions, electrons, X-rays and UV-photons. Studies of electron detection with silicon photodiodes have shown that electron-hole pairs produced in the contact layer can also contribute to the pulse of collected charge. SHCI do reach charge-state equilibrium in solids after only about 5–10 fs, and would thus deposit all their potential energy along a path of less than 10 nm in the contact layer. Attempts to quantify energy dissipation channels have almost exclusively focused on detection of secondary particles that are emitted from surfaces into the vacuum in the course of the interaction with SHCI. PIPS detectors thus offer the possibility of measuring the fraction of potential energy that is deposited in solids. First results from a study of the latter are described in Section 3.6.

2.7. X-ray detection techniques

Dispersive detection instruments for hard photons (X-rays in the energy region from 1 keV to nearly 100 keV), which have been employed in SHCI-surface measurements, can be divided into three categories: solid state detectors, crystal spectrometers, and calorimetric spectrometers. The differences in these photon spectrometers lies, in general terms, in their energy and time resolution, quantum efficiency and bandwidth, as well as their spatial efficiency.

2.7.1. Solid state detectors

Standard solid state detectors for X-rays are diodes of Si or Ge material. These have wide spread applications, because they cover a wide X-ray spectrum simultaneously with a high quantum efficiency, have a large detection area, have good time resolution and have high count rate capability and are commercially available. For detection of lower energy X-rays (1 keV to around 20 keV) a Li drifted p-doped Si wafer is contacted with a few tens of nm gold. Higher energy X-rays (2 keV to around 100 keV) are the domain of ultra-pure germanium detectors. The Ge water is contacted by ion implantation. The depletion zone (detection volume) is built up by applying a voltage of typically about 1 kV. For stability of the implanted and drifted wafer against diffusion under influence of the electric field the wafer needs to be cooled to liquid nitrogen temperature, and, thus, the detector has to be under vacuum.

When the photon is absorbed in the depletion zone, electron-hole pairs are created in a number proportional to the energy of the X-ray. The statistics of these electron-hole pairs determines the detector resolution ΔE. It varies therefore with $\Delta E \sim 150$ eV when the signal strength is far above the noise level. The typical values lie in the range of 120 eV and 220 eV at the energy of 5.89 keV, given by the Mn K_α line from β decay of an ^{55}Fe source. The low energy cut-off of the spectral range is determined by absorption in, most frequently, a Be vacuum window, the contact layers and the dead zone of the wafer. The high-energy cut-off is given by the photoabsorption in the depletion zone.

2.7.2. Crystal spectrometers

The crystal spectrometer, based on the X-ray defractive properties of crystals, is usually custom made. The use of focusing crystal geometry, together with the source and detector geometry, determine the type of crystal spectrometer (for example: van Hamos, Johan, plane crystal geometry). In the experiments with Ar^{17+} and Ar^{18+} ions [36], the dispersion of a flat crystal together with a linear position resolution-gas proportional counter with backgammon anode was used. The resolution which can be reached with such a spectrometer is better than 10^{-3}.

2.7.3. Calorimetric spectrometers

High resolution, large bandwidth and spectral efficiency are combined in calometric X-ray detectors [37]. In a micro-calorimeter the high-energy photons hit an absorber in which their energy is thermalized. This absorber material is weakly coupled thermally to a cold bath of typically 50 mK. The resulting rise in the absorber temperature is measured with a thermal sensor. In order to make the temperature rise measurably large, the material should possess a low heat capacity. With a proper choice of materials, the resolution of such a micro-calorimeter at 100 mK should in principle be 1 eV, independent of the X-ray energy. The absorber consists, in practice, of a high-Z superconducting material such as Sn, which has a low heat capacity, but high photo-absorption. In practice, the resolution is somewhat distorted by environmental noise. During the experiment reported here, where highly charged Ar ions hit a Be surface, a spectral resolution of 20 eV was reached, at a quantum efficiency of 90–100% in a range of 1–7 keV.

3. Experimental results

3.1. Charge equilibration time of SHCI in solids

Charge states of SHCI such as Xe^{44+} and Th^{75+} are far in excess of the mean equilibrium charge states that ions develop inside of solids. The later are $\sim 1+$ for velocities below the Bohr-velocity [38,39]. In this section, we review measurements of charge equilibration times of SHCI inside of solids. Equilibration dynamics in grazing incidence geometry are reviewed at the end of this section.

The de-excitation dynamics of SHCI in solids can be probed by measurements of Auger-electrons and X-rays, where characteristic energies are determined by the electronic configuration. Clock properties of hollow atoms have been explored by

Briand et al. [36] in measurements of X-rays from Ar^{18+} interacting with surfaces. Mean lifetimes of L-shell vacancies were found to be $\sim 10^{-16}$ s (see Section 3.4). Auger-electrons emitted following impact of Ne^{9+} on aluminum were measured by Grether et al. [40]. Here, the total equilibration time was estimated to be about 10 fs (see Section 3.3).

Measuring charge states of SHCI after transmission of thin foil targets allows for a rather direct determination of integrated de-excitation or charge state equilibration times. Using this technique, Schenkel et al. [39] found an upper limit of 21 fs for Th^{65+} (0.3 v_{Bohr}) in amorphous carbon. Expanding these measurements, Hattass et al. [41] used thinner foil targets (i.e., 5 nm or about 1 μg/cm^2) and observed non-equilibrium charge state distributions of SHCI after passage through solid matter. To the degree that initial velocities and foil thicknesses are known, these measurements allow for a direct determination of the time needed for SHCI to reach charge state equilibrium in solids. In the following, we describe these experiments in more detail. The experimental setup for charge state analysis in transmission geometry is described in Section 2.1.

Charge state distributions are shown in Fig. 4 for Th^{75+} after passage through 5 and 10 nm thick carbon foils. The initial velocity was 0.43 v_{Bohr}. A shift towards higher exit charge states is observed for the 5 nm ($q_{\mathrm{ave}} = 8.2+$) as compared to the 10 nm thick foil ($q_{\mathrm{ave}} = 2.9+$). The equilibrium charge state for thorium ions at this velocity is about 1.9+ [38]. Almost complete charge equilibration is

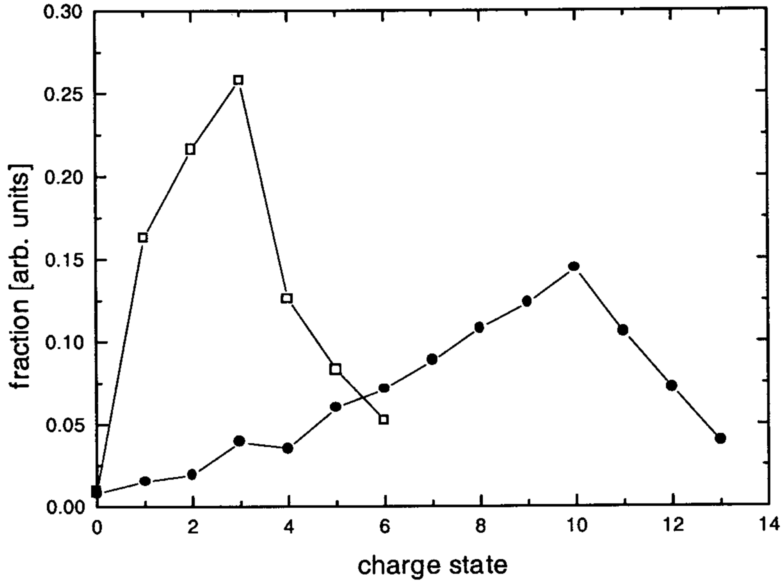

Fig. 4. Charge state distribution for Th^{75+} after passage of thin carbon foils. The initial velocity was 0.43 v_{Bohr}. Open squares represent data for passage through 10 nm foils; solid circles represent data for passage through 5 nm thick foils. Lines drawn to guide the eye.

accomplished in the 10 nm foil, during a time of 10 fs. On the contrary, the time of 5 fs that ions spend in the 5 nm foil is too short for complete de-excitation.

In this experiment, transmitted projectiles are detected after flight times of a few microseconds, long enough for the decay of any surviving inner-shell vacancies. Fluorescent yields for thorium M-shell vacancies are ~0.1 [42], and most vacancies decay through Auger transitions. In an estimated upper limit, the projectile charge state increases by +3 in the course of cascading processes outside the solid [43] following the filling of each surviving M-shell vacancy. For fully equilibrated projectiles, where all inner shell vacancies are filled inside the solid, exit charge states 1+ and 2+ could stem from loss of loosely bound electrons (via Auger processes) when ions exit the foil [43]. Electronic configurations of transmitted projectiles can not probed directly in this experiment. However, charge state distributions in Fig. 4 are consistent with the presence of at average less than one M-shell vacancy after passage of the 10 nm thick foil, while for the 5 nm foil at average about 2 of the initial 13 M-shell vacancies of Th^{75+} survive.

Fig. 5 shows q_{ave} for Xe^{44+} versus projectile velocity, v, ranging from 0.23 v_{Bohr} to 0.43 v_{Bohr}. The dotted line gives a comparison to calculations of mean equilibrium charge states, q_{eq}, using Bohr's stripping criterion ($q_{eq} = Z_{ion}^{1/3} \times v_{ion}/v_{Bohr}$) [38,43,44]. Values for q_{ave} show only a weak increase for the 10 nm thick foil, in reasonable agreement with values calculated using the Bohr formula.

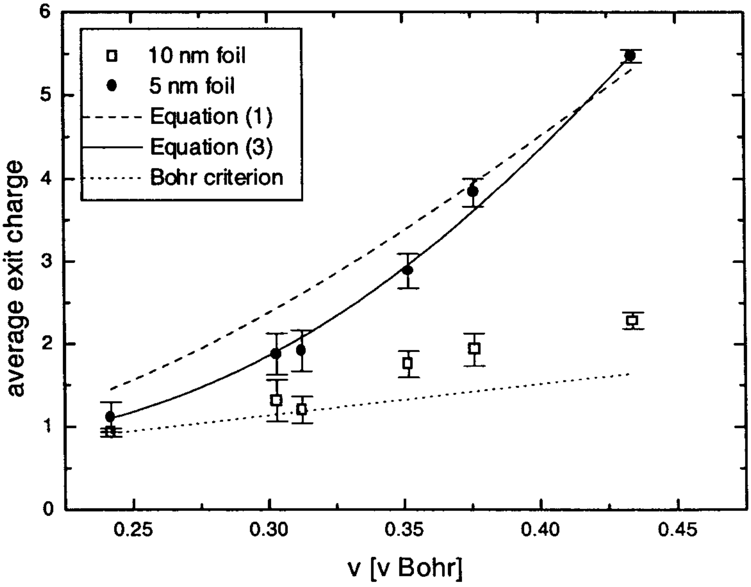

Fig. 5. q_{ave} of Xe^{44+} ions after transmission of thin carbon foils vs initial projectile velocity. Open squares represent data for passage through 10 nm foils, solid circles represent data for passage through 5 nm foils. Dotted line: Bohr criterion; dashed line: Eq. (2); solid line: Eq. (4) [41].

However, the q_{ave} for the 5 nm foil increase significantly, indicating incomplete equilibrium once the time spent inside the foil is reduced below about 7 fs.

An approach to describe the development of ion charge states in solids has to consider two contributions: the response of the electronic system of the target and pertinent atomic collision parameters [1,43,45]. In a rigorous treatment, non-linear screening has to be considered and knowledge of cross sections for multiple electron capture processes is required. In a simple linear response approximation [46], Hattass et al. [41] assume that de-excitation follows an exponential decay from the initial charge state, q_{i}, to the equilibrium charge state, q_{eq}. The approach to equilibrium is then given by:

$$q(x) = q_{\mathrm{eq}} + (q_i - q_{\mathrm{eq}})\mathrm{e}^{-\alpha x/v} \tag{2}$$

Here, x is the depth coordinate and α is an equilibration rate comprised of contributions from the electronic response of the solid, λ, i.e. the inverse relaxation time of the electron gas [47,48], and a de-excitation rate averaged over multiple atomic transitions, γ. q_{eq} was calculated for each velocity from Bohr's stripping criterion. A least-square fit for Xe^{44+} to this formula (Fig. 5) yields a value of $\alpha = 4.7 \times 10^{14}\ \mathrm{s}^{-1}$.

The fit obtained when assuming a simple exponential decay describes the general trend of data in Fig. 5. However, the agreement is much improved when the influence of electronic response of the target electronic system and atomic transition rates are treated separately. In this scenario, screening is not complete immediately after projectiles enter the solid, but requires a finite build-up time. Transition rates for the filling of inner shell vacancies are then limited by the number of electrons in the screening cloud. Once the population of screening electrons saturates, neutralization proceeds again by simple exponential decay.

This can be expressed in a first-order linear differential equation:

$$\frac{\mathrm{d}q}{\mathrm{d}t} = -\gamma(1 - \mathrm{e}^{-\lambda t})q \tag{3}$$

With boundary conditions $q(t=0) = q_i$ and $q(t=\infty) = q_{\mathrm{eq}}$ and setting $t = x/v$ it follows that:

$$q(x) = q_{\mathrm{eq}} + (q_i - q_{\mathrm{eq}})\mathrm{e}^{-\gamma\frac{x}{v}}\mathrm{e}^{-\frac{\gamma}{\lambda}\left(\mathrm{e}^{-\lambda\frac{x}{v}} - 1\right)} \tag{4}$$

A fit to this formula (Fig. 5, solid line) gives $\lambda = 4.3 \times 10^{14}\ \mathrm{s}^{-1}$ and $\gamma = 7.6 \times 10^{14}\ \mathrm{s}^{-1}$ for Xe^{44+}.

Typical filling times for inner shell vacancies in hollow atoms are $\sim 10^{-16}$–10^{-15} s [49,50]. The finding of charge equilibration times of only ~7 fs demonstrates that multiple transition cascades have to proceed in parallel to facilitate this rapid de-excitation. The concept of a built-up time or electronic response time of about 2 fs has to be validated in measurements with target materials with different electronic response functions.

Measurements of neutralization of SHCI have also been carried out in grazing incidence geometry [1]. Winecki et al. [17,51] have observed very efficient neutralization for C^{q+}($q=2$, 4, 6), Ar^{q+}($q=4$–17), and Fe^{q+} ($q=5$, 10, 15, 22) scattering from a graphite surface at grazing incidence. The final charge state of the projectile is independent of the initial charge state and only dependent on the projectile velocity, i.e. the projectile reaches charge state equilibrium during the encounter. The key point here, as in the carbon foil experiments discussed above, is that the carbon substrate does not have occupied orbitals with sufficient energy overlap to directly populate (side feeding) the inner shell vacancies (K- and L-shell of the projectile). These authors model the neutralization with side feeding into intermediate shells (M-shell for Ar) and subsequent Auger and radiative transitions to fill the inner shells. They find the atomic transitions rates are sufficient to allow complete filling of the inner shells. This model points to the electron gas density of the surface as the cause of the neutralization.

Huang et al. [18,52] have also observed very efficient neutralization for large angle scattering (incident angle 25°, exit angle 75°) for slow highly charged argon ions scattering from a Au(111) surface. For all initial charge states ($q=6$, 7, 9, 11, 13, 15), at least 50% of the scattered particles were found to be neutral. This is remarkable since the projectile scatters at one Au atom. However, very strong shell effects in the neutralization were, nevertheless, observed. For Ar^{7+} the yield of multiply charged scattered ions is about three orders of magnitude lower than that of singly charged scattered ions. However, when the incident ion carries one or more L-shell vacancies ($q \geq 9$), the yield of multiply charged scattered ions increases by two orders of magnitude. This is a much larger effect than observed in grazing scattering (a factor of two) [1,17]. This discrepancy (the strong shell effect) could be attributed to the short time the large angle scattered projectile spends near the surface on the out-going trajectory, i.e., L-shell filling is incomplete when the ion leaves the surface.

Meyer et al. [53] have investigated neutralization of single and multiply charged ions on insulator surfaces (LiF) in grazing incidence. Surprisingly, a significant enhancement in the neutral fraction was observed for the multiply charged ions compared to the singly charged ions. This effect was interpreted as arising from the blocking of neutralization of the singly-charged projectiles due to the lack of available levels quasi-resonant with the target valence band, and the bypassing of this bottleneck by the multiply charged projectiles via capture into excited states which can relax by Auger de-excitation. For metals this effect is not observed. For the multiply charged projectiles, no effect of initial charge state on the final charge state was observed, i.e., complete neutralizations was achieved.

3.2. Charge state dependent energy loss

Energetic ions traveling in solids lose kinetic energy in collisions with target electrons and nuclei [38,54,55]. Energy loss is a function of the projectile charge state in the solid [56–58]. As we have seen in the previous section, charge states of SHCI are far in excess of their mean equilibrium charge state in solids.

Consequently, the finite de-excitation time (Section 3.1), τ_{eq}, should result in pre-equilibrium contributions to energy loss processes along a charge state equilibration length, Δx_{eq} [59].

Schenkel et al. [60,167] have measured the energy loss of slow ($v=0.3\ v_{Bohr}$), SHCI transmitted through thin foils using TOF spectrometry (see Section 2.1 for experimental details). The dependency of energy loss on projectile charge is shown in Fig. 6. Here, a constant velocity of 0.3 v_{Bohr} was used for ions of all species and charge states. Projectiles and initial kinetic energies were: ^{86}Kr, 197.7 (±1); ^{136}Xe, 312.4 (±2) keV and ^{197}Au, 454.4 (±3) keV. Using a thinner target, lower ion velocities and higher charge states, these results extend the studies of Herrmann et al. [61], where no effect of incident ion charge on energy loss was found for ions up to Ar^{16+}, to a regime where the onset of charge effects can be observed. Juaristi and Arnau [62] performed density functional theory calculations predicting a decreasing energy loss in the presence of one K-shell vacancy in oxygen ions. However, these results can only be tentatively compared, since calculations considered only electron-hole pair excitations of target valence electrons at the Fermi level as mechanisms for energy loss. Unfortunately, the experimental technique does not allow differentiation of inelastic and elastic contributions to energy loss processes.

For xenon- and gold-ions, ΔE_{ave} increases strongly with charge. Energy loss in the foil is the sum of contributions to stopping processes before, $(dE/dx)_{pre}$, and after, $(dE/dx)_{eq}$, a dynamic charge-state equilibrium is established. Both

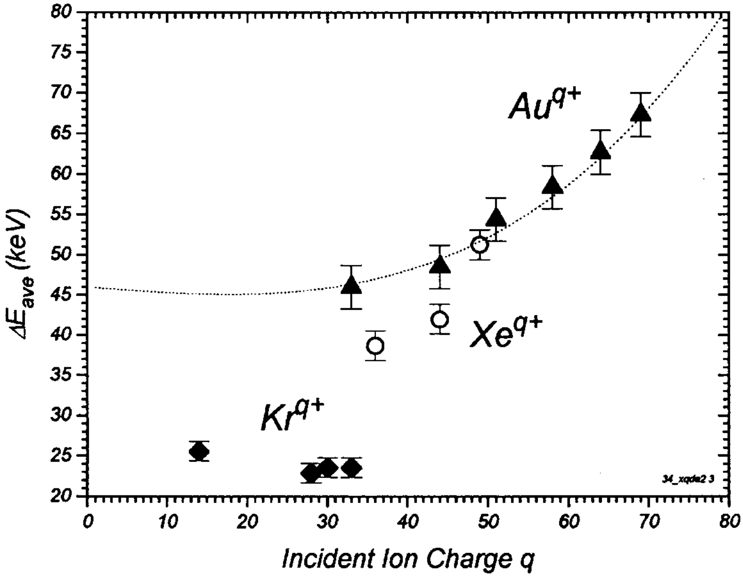

Fig. 6. Average energy loss of Kr$^{14,28,30,33+}$, Xe$^{36,44,49+}$, and Au$^{33,44,51,58,64,69+}$ in a thin carbon foil [60,167].

equilibration length, Δx_{pre}, and pre-equilibrium stopping power, $(\mathrm{d}E/\mathrm{d}x)_{\mathrm{pre}}$, are a function of the projectile charge state, q. In an attempt to estimate values for Δx_{pre}, τ_{eq} and pre-equilibrium stopping power enhancements, Schenkel et al. [60,167] assume a simple power law dependency of Δx_{pre} and $(\mathrm{d}E/\mathrm{d}x)_{\mathrm{pre}}$ on q. With values for de-exciting times from measurements of charge state distributions of transmitted ions, the resulting increases of pre-equilibrium over equilibrium stopping powers during de-excitation are a factor 2 along an equilibration length of 4–5 nm ($\tau_{\mathrm{eq}} \approx 7$ fs). In the absence of a critical number of inner shell vacancies, for example for ions like Kr^{33+}, de-excitation processes at and below the surface are too fast ($\tau_{\mathrm{eq}} \leq 1$ fs, $\Delta x_{\mathrm{pre}} \leq 0.7$ nm) and pre-equilibrium stopping power increases are too weak ($\mathrm{d}E/\mathrm{d}x|_{\mathrm{pre}} < 2\ \mathrm{d}E/\mathrm{d}x|_{\mathrm{eq}}$) to allow for strong contributions to energy loss processes before de-excitation is completed.

The interaction of SHCI with solids can be described in terms of hollow atom formation above and below the surface [1,2]. Inside the solid, neutralization of the projectile charge by a screening cloud of target electrons requires an extreme degree of target polarization, involving over ten carbon atoms to provide the charge required to neutralize a Au^{69+} projectile. Inside insulating targets, a lack of free electrons inhibits efficient screening of projectiles and Biersack had suggested that this reduced screening results in pre-equilibrium energy loss enhancements due to long-range Coulomb interactions [58] between projectile nuclei and ionic cores [15]. Evidence for this effect was observed by Briere et al. [15] who measured a higher energy loss for Ar^{16+} when passing through the $\mathrm{CaF_2}$ layer rather than the carbon layer in a thin (~15 nm) $\mathrm{CaF_2}$-carbon bi-layer foil target. Au^{69+} on carbon represents an asymmetric combination of a heavy projectile incident on a light target. Here, direct filling of M-shell vacancies in gold projectiles by target electrons is strongly inhibited. Only projectile levels with principal quantum numbers $n \approx 6$–10 can be populated directly. The charge distribution in the hollow atom is characterized by electrons in the initially filled K- and L-shells and by electrons in highly excited states. Intermediate levels with $n \approx 3$–5 are filled in the course of de-excitation. Screening of the projectile nuclear charge is reduced at distances from the nucleus equal to the radii of these empty levels. Averaging over all impact parameters, this can be interpreted as an increased effective charge of hollow atoms. Scaling of the electronic stopping power with the square of an effective ion charge was proposed to estimate charge state dependent electronic stopping power increases for slow, highly charged ions [58,61]. Effective charge theory is a semi-empirical parameterization that has been applied successfully to the systematization of energy loss data for heavy ions at intermediate energies (~MeV/u). The usefulness of the theory for conceptual adaptation to collisions in the deeply adiabatic velocity regime presented in this study is consequently rather limited. At atomic transition rates in the order of 10^{15}–10^{16} s^{-1}, screening of the nuclear charge and the interaction potential between projectile and target nuclei change on the time scale of individual collisions (~0.5 fs). Momentum transfer to target electrons and nuclei in collisions with impact parameters comparable to the radii of unoccupied levels in the transient hollow atom is increased over corresponding values for projectiles in equilibrium. The complexity of charge changing dynamics has—so far—limited more refined theoretical treatments of charge state effects on (electronic) stopping, such as density functional theory, to hydrogen and helium ions in free electron metals [63,168]. The effect of K-shell vacancies has been approached recently as described [62].

Energy loss has also been measured for ions reflected from surfaces. Khemliche et al. [64] have observed an enhanced energy loss for N^{7+} compared to N^{6+} for scattering from an Al(110) surface. This result is in contradiction to the prediction of Arnau [65] that the stopping power would decrease with increasing number of K-vacancies for nitrogen projectiles impinging on an aluminum surface. Uncertainties in the measurement stem from the effect of the image charge acceleration (change of the scattering trajectory) and the plasma source potential (change of the initial energy). Very recently, this controversy was addressed in a detailed experimental and theoretical study by Juaristi et al. [67].

Winecki et al. [66] have shown the energy loss for highly charged argon ions ($Ar^{2,16+}$) at grazing incidence on a graphite surface to be very sensitive to the angle of incidence. They have observed a weak influence of the initial charge state of the projectile on energy loss, which can be explained by the image charge acceleration in front of the surface. Apart from this effect, energy loss for highly charged argon ions does not depend on the initial charge state of the projectile. The energy loss results agree with the predictions by a modified Firsov model [54,67,166] when the image charge acceleration is considered.

Using a similar modified Firsov model with electron capture, Auger transitions, and image charge acceleration, Huang et al. [16] were able to describe many of the features of the energy loss for large angle scattering of Ar^{9+} from a Au(111) surface. Both Huang et al. [16] and Winecki et al. [66] came to the same conclusion that neutralization and inelastic energy loss occur during the incoming trajectory for both grazing geometry and large angle scattering geometry. Interestingly, a correlation between inelastic energy loss and exit charge state is observed for the large angle scattering. However, the change in energy loss with exit charge state is less than 2% of the energy loss.

3.3. Electron emission

Since the potential energy of the HCI is transferred to the solid surface on the femtosecond time scale (see Section 3.1), the electronic system of the surface is the initial recipient of the energy. One probe of the electronic response is the energy and yield of the emitted electrons. The dynamics of the energy transfer process can be followed to some extent by monitoring the electron emission as a function of the velocity and the angle of incidence of the HCI. The research groups at the Hahn-Meitner-Institut, Technische Universität Wien, Westfälische Wilhelms-Universität Münster, Lawrence Livermore National Laboratory, and the Rijksuniversiteit Groningen have made progress in understanding the dynamics by these methods.

Khemliche et al. [68] have studied the KLL-Auger spectrum arising from grazing incidence 6 keV O^{7+} projectiles as a function of LiF coverage (up to one monolayer) on a Au(111) substrate. The astonishing similarity, with respect to KLL-Auger emission, between a single LiF monolayer on Au(111) and a LiF bulk surface indicates that the large band gap of the latter is not the limiting factor in above surface neutralization of highly charged ions. On the clean Au(111) substrate Auger peaks at 467 and 481 eV are observed for O^{7+} which have been assigned to a slow L-shell filling process above the surface. The intensity of these peaks is a direct signature of the efficiency of the above surface neutralization. On the bulk LiF surface and the one monolayer LiF on Au(111) the intensity of the 467 and 481 eV peaks are greatly reduced if not entirely removed, suggesting the above surface neutralization is much less efficient for these surfaces. The one monolayer LiF film does not have the large bandgap of the bulk LiF surface, but does retain the high electron binding energy of the F(2p) electrons. The large bandgap of the bulk LiF surface should prevent captured electrons from being lost into target empty states, suppressing the L-shell filling above the surface. However, since the monolayer LiF surface exhibits the same Auger spectrum as the bulk LiF surface, the effectiveness of resonant electron loss as a speeding-up mechanism in the filling of inner shells is questioned.

In another exciting advance, Niemann et al. [69] have reported evidence for the creation of both surface and bulk plasmons due to the neutralization of multiply charged neon ions, $q = 1\text{-}6+$. The decay of the plasmon induces an electron that may escape from the surface. The plasmon creation signal is observed as electrons emitted at 6.5 and 11 eV, which correspond to surface and bulk plasmons, respectively. As a primary mechanism for plasmon production, the capture of a conduction band electron into the L-shell of the Ne projectile provides the excess energy for plasmon creation similar to the mechanism proposed by Baragiola and Dukes [70]. An important point is the resonance requirement for the plasmon production. Due to energy conservation, the energy required for plasmon creation must be close to the potential energy liberated by the projectile. For the bulk Al plasmon the resonance condition is 15–20 eV and is fulfilled by Ne with a single vacancy in the 2p orbital if the captured electron comes from the screening cloud. For highly charged ions the resonance condition will only be reached at the end of the neutralization process. The probability for multiple plasmon production to accommodate higher potential energy transfers is not addressed.

Lemell et al. [21] measuring number statistics of emitted electrons in coincidence with projectile scattering have demonstrated that they can separate potential from kinetic electron emission. Using this technique they have determined that for Ar^{8+} scattering from Au(111), potential electron emission occurs above the surface and is independent of parallel velocity by comparison to previous normal incidence measurements [1]. For these very low perpendicular energies (137 eV) and for projectiles with no K- or L-shell holes, it is likely that neutralization occurs entirely above surface.

Diez Muino et al. [71] have used density functional theory to calculate the rate of LCV Auger processes for the interaction of Ne and N ions with Au and Al substrates. In this LCV Auger process, the final localized state is an L-shell state bound to the ion; the initial continuum (C) electronic state is centered around the ion (the screening cloud); and the extended valance (V) electron states respond in the process in providing electron-hole pair and plasmon excitations. These rates are close to those required to explain the experimentally measured Auger spectra [1,40].

Diez Muino et al. [72] and Arnau [73] have continued to develop the use of density functional theory to describe the screening of the HCI by an electron cloud from the valance band. The calculated L-Auger transition rates for Ne^{9+} in a free electron gas (Au electron density parameter $r_s = 1.5$ or Al $r_s = 2.0$) are the same order of magnitude as those obtained for isolated atoms. They obtain atomic-like rates only because the screening cloud has atomic-like character. Calculated rates without the perturbation of the target electrons are an order of magnitude slower. This result is in accordance with the findings of Hattass et al. [41] that the neutralization time is roughly similar to the linear response theory predicted screening time (see Section 3.1). The radiative recombination rates for K-vacancies in Ar^{17+} in a free electron gas show a large influence (increased rate) of the nonlinear distortion of the valance band.

Niemann et al. [74] have measured the yield and kinetic energy of the low energy electrons emitted when N^{6+} ions impact a Au surface. A single stage spectrometer was used to obtain reliable (absolute error ±50% for energies less than 10 eV) electron measurements down to a few eV. The kinetic energy of the projectile was varied between 90 eV and 60 keV. At low kinetic energy (90 eV) the time spent above the surface is long enough that nearly all of the electron emission per primary ion can be accounted for by above surface processes. However, even in this case, the K-shell vacancy is not filled 90% of the time until the ion penetrates the surface. For 270 eV projectiles the K-shell is not filled 99% of the time until the ion penetrates the surface. Interestingly, for 60 keV projectiles nearly all of the electron emission is a result of below-surface processes (i.e., the time spent above surface is too short for substantial electron emission).

In more recent work by Niemann et al. [75], the angular distribution of the emitted electrons is measured for Ne^{9+} ions impinging on an aluminum surface. The measured angular distribution contained a constant portion and a cosine θ dependent portion, where θ is measured with respect to the surface normal. The low energy electrons were nearly independent of emission angle, whereas, the higher energy emission was more angle-dependent. The interpretation suggested by these results is that the low energy (~4 eV) emission occurs above surface or at the surface, whereas, the higher energy emission occurs below the surface. The higher energy emission originating below the surface and emitted at grazing exit angle will travel through cosine θ more aluminum surface before exiting than electrons emitted along the surface normal.

Grether et al. [40] have also studied the KLL and LMM Auger electron emission for Ne^{9+} impinging on Al as a function of projectile energy in the range of 0.1–22.5 keV. The structure of the KLL maximum change dramatically with impact energy due to the onset of charge transfer between target Al and projectile L-shells. At the lowest velocities the L-shell has low occupation numbers ($n_L = 2$–

3) and hence the K-Auger electron emission is dominated by KL_1L_1 transitions. At higher velocities, the charge transfer cross sections increase leading to larger L-shell occupation numbers ($n_L \geq 4$) and hence the K-Auger electron emission reveals much larger contributions from $KL_{2,3}L_{2,3}$ transitions. L-Auger electron emission decreases very quickly with projectile energy. This is due to two effects. First is the L-shell holes are filled by charge transfer from the target Al to the projectile. The charge transfer cross sections increase with velocity. Second is the attenuation of the electron emission with depth of origin in the solid surface. The inelastic scattering of these low energy electrons limits the depth from which these electrons can escape. The results were described by a 'cascade' model for the filling of the hollow atom. The cascade model predicts the lifetime of the K-shell hole in this case to be about 10 fs in good agreement with the neutralization measurements presented in Section 3.1.

Ducree et al. [76,77] have made a very exciting observation of an Auger electron transition they have labeled KLV_w. The V_w refers to the resonant Rydberg level for above surface charge transfer. While the quantum number for his state evolves the energy remains at the target work function, W. This transition is only observed at very low perpendicular velocities of the projectile (i.e. grazing incidence and $\sim$10 eV × q) and for metastable projectiles such as metastable C^{4+} (1s2 s) or metastable Ar^{8+} (1 $s^2$2 $s^2$2$p^5$3 s). The metastable configuration is required so that a 2 s or 3 s electron can fill the K- or L-shell hole, respectively, before bulk surface penetration. The low perpendicular velocity is required because of the low transition rate for this feature. This result appears to be in contradiction to the above-surface cascade model, which has been invoked previously to explain the increase in above-surface potential electron emission with decreasing perpendicular velocity [22]. The KLV_W transition suggests that many of the captured electrons remain in the V_W level in the above-surface interaction phase, otherwise one might expect to observe this feature in non-metastable projectiles, like C^{5+} or Ar^{9+}, which is not the case. In accordance with other measurements described above, Ducree et al. [76,77] were also able to show that the dominant L-Auger emission originates from inside the surface for Ar^{9+} and metastable Ar^{8+} impinging on Si(100). They also present indirect evidence for very effective MCV Auger filling transitions inside the surface, where (C) refers to the screening cloud induced by the ion inside the surface.

Thomaschewski et al. [78] have studied KLL Auger emission eliminating subsurface contributions for N^{6+} on Au(111). Subsurface emission was removed from the measurements by using grazing incidence trajectories where all the projectiles are reflected by the first atomic layer. It was shown by Doppler shift analysis of the electron energies that emission from the hollow atom states (incomplete L-shell) occurs after image charge acceleration of the projectile but before it is reflected from the surface, and the emission with filled L-shell occurs after reflection. Utilizing the refraction of the emitted electron by the surface potential barrier, the height of emission could also be assessed. The unfilled L-shell Auger emission ($n_L = 2$) occurred higher above the surface than the nearly-filled L-shell Auger emission ($n_L = 5$–6).

In an extension of their previous work on N^{6+} on Au(111), Thomaschewski et al. [79] demonstrate that penetration of the first atomic surface layer does not significantly change the observed K-Auger emission. The K-Auger emission is deconvolved into substantially unfilled L-shell ($n_L = 2$) emission and nearly-filled L-shell ($n_L \geq 3$) emission. The L-shell filling is smoothly dependent on the perpendicular velocity of the projectile and not on trajectories penetrating the first atomic layer. They conclude that the appropriate definition of the surface in this case is the border of the electron gas.

In another study utilizing the non penetrating nature of grazing incidence trajectories, Morosov et al. [80] have measured the correlation between the emission of K-Auger electrons and the low energy secondary electrons for O^{8+} and O^{7+} impinging on a LiF crystal surface. The low energy secondary electron yield increased with decreasing number of K-Auger electrons observed. The implications is that K-Auger electrons emitted toward the surface, but that do not escape, produce a measurable (the number of low energy electron is increased by 3 per projectile) increase in the secondary electron yield.

Hägg et al. [81] and Ducree et al. [82] have used the *classical-over-the-barrier* (COB) model and an extended, dynamical COB model, respectively, to investigate the above surface neutralization of slow, highly charged ions in front of ionic crystals. The major differences between ionic crystal surfaces and metal surfaces are the large work function, the large band gap and the dielectric response. The COB model as formulated by Hägg et al. [81] predicts that the effects of the increased work function will dominate the effects due to the dielectric response. For example, the critical distance for first capture will be much closer to the surface and the principal quantum number at first capture will be significantly smaller for an ionic crystal surface as opposed to a metal surface. The dynamical COB predicts similar effects, but also includes local surface charges. The effects of increased work function seems to be balanced by the dielectric response and local surface charging to produce a similar energy gain for SHCI approaching metal or insulator surfaces. Energy gain due to the polarization of the surface (image acceleration) is in agreement with recent experimental values for SHCI on LiF [83].

Schenkel et al. [19,164] using a pulse height distribution method (see Section 2.2) have compared the relative secondary electron yield for hydrocarbon covered Au(111) and an SiO_2 (150 nm on Si) surface as a function of incident ion charge from 1+ to 75+. For $q > 5+$ the secondary electron yield was always smaller for the SiO_2 surface than the gold surface, reaching a factor of two for Th^{75+} primary ions. A possible explanation for the lower secondary electron yield of the SiO_2 surface could have been the different work functions of the material (~11 eV for SiO_2 versus ~5 eV for gold). However, in an extension of this work Niedermayr et al. [84] have shown that clean graphite and clean gold surface with the same work function have different secondary electron emission yields. Higher yields are observed from the highly-oriented pyrolytic graphite surface than from the clean gold surface. The dielectric response and/or the plasmon response of the surface may play a larger role in the subsurface emission than the work function.

This is just the opposite of what was reported for the calculations for above-surface response.

Good summaries of the electron emission mechanisms and considerations were given by Stolterfoht et al. [85] and Lemell et al. [86].

3.4. X-ray emission studies

Hollow atoms for high Z, highly charged ions ($Z > 18$) have been studied mostly by means of X-ray spectroscopy, while Auger electron spectroscopy is used mostly for lighter SHCI. Hollow atoms are produced via charge transfer from the surface to the ion which starts when the potential barrier decreases below the value of the work function W. The formation of hollow atoms can be described according to the '*over-barrier-model*' (OBM) at relatively large distance from the surface (approximately at $d_c \approx \sqrt{(2q)}/W$ (a.u.)). The OBM predicts also that electrons start to be transferred from the surface into Rydberg states n of equivalent energy, i.e. $n \approx q/\sqrt{W}$ (a.u.). One can prepare a 'hollow atom' in different configurations. For example, Ar^{9+} on Au has $d_c = 22$ a.u. into $n = 10$, and U^{92+} on Au has $d_c = 65$ a.u. into $n = 100$. 'Hollow atoms' are complex multiply excited atoms with vacancies in the inner most shells and electrons in quasi-stationary high Rydberg states.

The Auger or photon cascades, which could fill the inner levels of the 'hollow atom,' are, however, too slow compared to the time the ion spends above surface. The ion is still in a highly excited state when it reaches the surface. The time between first electron capture and impact on the surface can be controlled by varying the approach velocity of the ion. A lower limit for the approach velocity is given by the image charge acceleration. When a slow highly charged ion approaches a metallic or insulator surface with a given dielectric constant, a negative image charge is formed on the surface, which provides an attractive potential. This results in an acceleration of the ions during the approach towards the surface plane. A calculation based on the OBM produces an energy gain: $V_{\text{im}}^{q+} \approx -(W/4)(q^{3/2})$. This formula has been tested in scattering experiments [87] and by electron emission measurements for highly charged ions [22]. With the work function $W \approx 4$ eV for a metal surface the image energy is $V_{\text{im}}^{q+} \approx 30$ eV for $q = 10$.

When the ion starts to penetrate into the bulk high-n electrons of the hollow atom are stripped off. Closer collisions with lattice atoms change the structure of the hollow atom into a 'hollow atom of a second kind'. The transfer of electrons occurs into lower states (e.g., via so called 'side feeding' [88]). The n values depend on matching energy levels in the ion and the solid. From these lower n states electrons can cascade into inner-shell vacancies giving rise to hard X-rays. The ion relaxes until it reaches its equilibrium charge state after a few layers. The time period from first electron capture to the complete relaxation is in the order of femtoseconds. Within this time the total energy of the ion is deposited. In most of the measurements, the X-rays from transitions in 'hollow atoms of a second kind' have been observed [2,36,89–95]. An additional process that fills inner shell states directly inside the solid is an Auger transition from the conduction or valence band into inner shell states of the ion. The importance of this Auger neutralization process was already predicted by Hagstrum [96]. Both the dynamics of the neutralization process and the atomic structure of the multiply-excited hollow atoms present challenging many-body problems. Atomic structure calculations used to explain the measured electron and X-ray spectra have usually

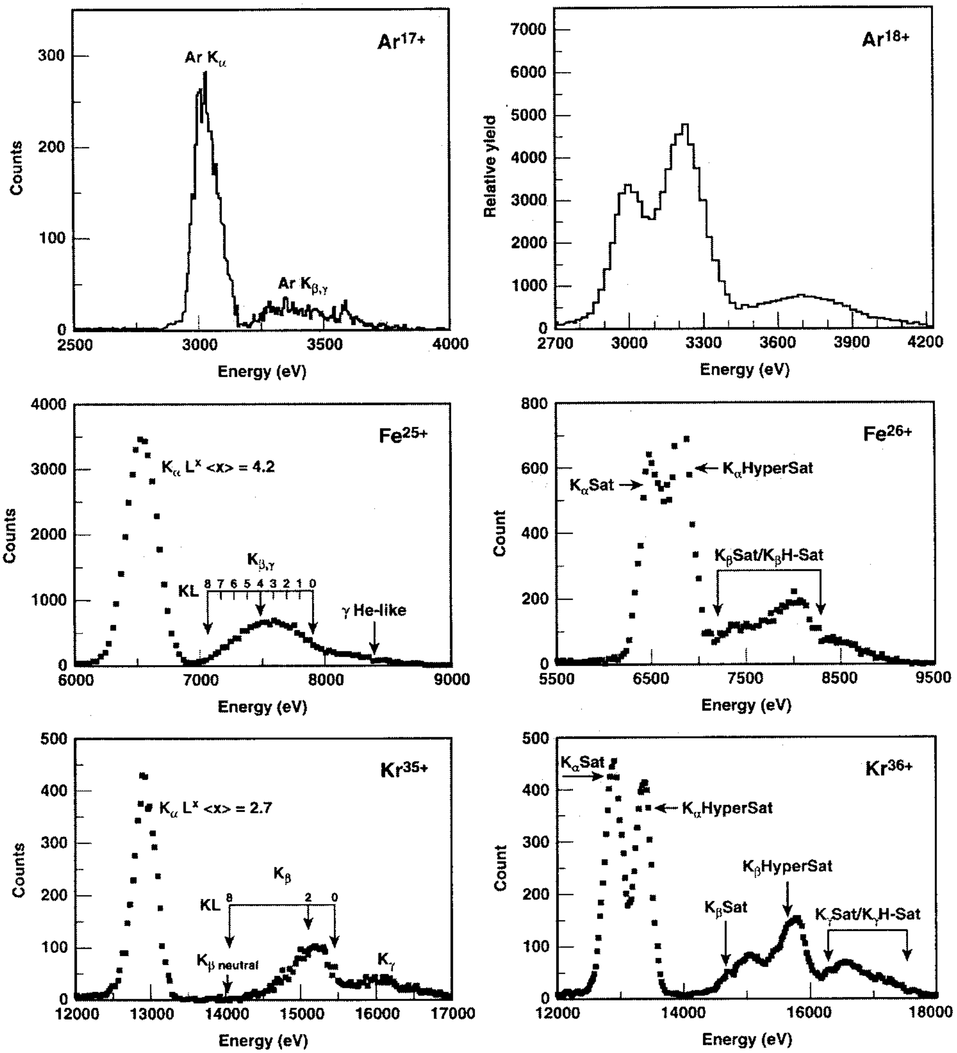

Fig. 7. Overview of X-ray emission spectra following H-like and fully stripped Ar^{q+}, Fe^{q+}, and Kr^{q+} ions incident on solid surfaces. The Ar^{17+} spectrum has been measured using a calorimeter detector. All other spectra were measured using Ge solid state detectors.

treated atomic states in vacuum instead of considering crystal fields and induced fields from conduction and valence electron screening at the solid surface or inside the bulk.

In a variety of experiments the time evolution between the population of the outer shell states and subsequent decay of the inner shells has been studied. Using high-resolution X-ray spectroscopy, satellite lines (e.g., KL^n lines from one K-shell vacancy and n electrons in the L-shell) can be observed. Energies and intensities depend on the vacancy configuration at the time of a radiative relaxation. If one knows the initial configuration from measurements on monatomic targets then the K X-ray emission following surface interactions can act as a clock, revealing electron rearrangement times on a time scale of 10^{-16} s.

3.4.1. K-shell X-ray emission

Ar K X-ray emission following the impact of $Ar^{17+,18+}$ ions over a wide range of impact velocities on a variety of surfaces have been investigated systematically [36,50,90–93,97].

Investigations of hollow atom formation above insulators as compared to metals have revealed detailed information on de-excitation processes [1,64,68,80,81,83,92,97,170,171]. The possible backscattering of very slow highly charged ions from insulator surfaces following charge built up on the incident trajectory has stimulated both controversial discussions [92,170,171] and ongoing investigations [97].

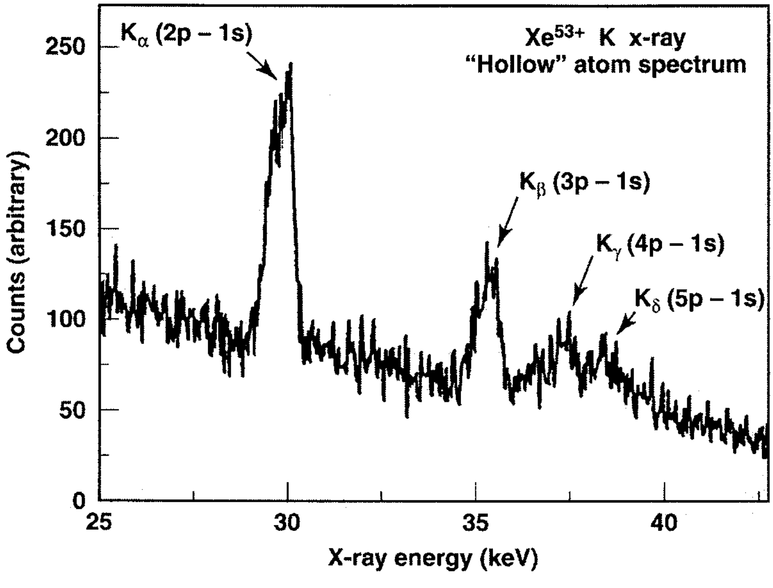

Fig. 8. K X-ray emission spectrum from the radiative de-excitation of 357 keV Xe^{53+} ions incident on a Au target.

Figs. 7 and 8 show a series of K X-ray spectra from H-like and bare Ar, Fe, Kr and Xe ion impact on metallic surfaces. No distinction between any above or below emission of K X-rays can be made from the observation of these spectra. It is assumed that the emission of these spectra results predominantly from the radiative de-excitation below the surface. The fact that even the highest charged ions are neutralized within fs in a few nm raises the question what processes are responsible for the fast neutralization and filling of the inner shell vacancies. Resonant neutralization, side-feeding, Auger neutralization, electron promotion (or ‘demotion’) are considered on the basis of level matching conditions as illustrated in Fig. 9. Characteristics of K X-ray emission are used to analyze the filling times.

The Auger neutralization model was developed to understand the interaction of singly charged ions with surfaces. It assumed that, inside the solid at very low velocities, the ions may form a transient molecular compound with few target atoms. The model also assumed that electron transfer from the atoms of the solid to the excited states of the ion is accompanied by the emission of another electron into the continuum to ensure energy conservation. Such a model may be extended for highly charged ions and for the filling of inner shell vacancies. Through an Auger neutralization process, K-shell electrons of C-target atoms may be able to directly populate deeper excited levels of highly charged projectiles than predicted by the resonant transfer model. One target electron of the K-shell of carbon fills

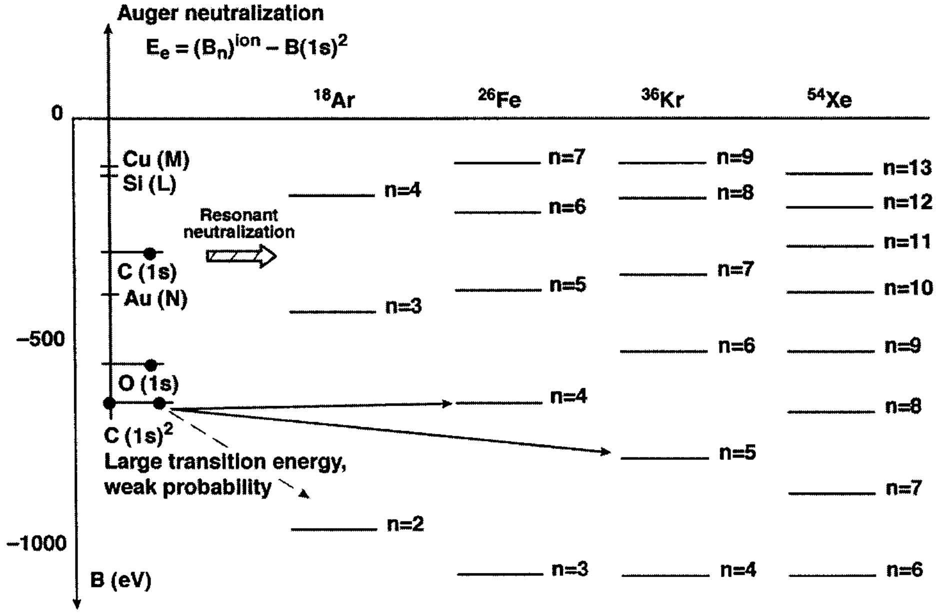
Auger neutralization
$E_e = (B_n)^{ion} - B(1s)^2$
^{18}Ar
^{26}Fe
^{36}Kr
^{54}Xe
0
-500
-1000
B (eV)
Cu (M)
Si (L)
Resonant neutralization
C (1s)
Au (N)
O (1s)
C (1s)^2
Large transition energy, weak probability
n=4
n=3
n=2
n=7
n=6
n=5
n=4
n=3
n=9
n=8
n=7
n=6
n=5
n=4
n=13
n=12
n=11
n=10
n=9
n=8
n=7
n=6

Fig. 9. Selected energy levels for a number of target materials (C, O, Cu and Au) in comparison to levels in hydrogen-like Ar, Fe, Kr and Xe ions.

the inner shell of the ion while a second electron is ejected into the continuum. The Auger transition rate being maximum when the energy of the ejected electron is minimum, this process is then strongly selective for the level population of the ion.

By comparing the mean time for the filling of one L-vacancy in hollow atoms with the LMM Auger rate, it might be possible to get qualitative information on the relative importance of the side feeding of $n > 2$ levels and on the filling of the L-shell by the Auger decay.

The radiative de-excitation of 7 kV/q Fe^{25+}, Fe^{26+}, Kr^{35+}, Kr^{36+}, and Xe^{53+} and Xe^{54+} ions was measured by Briand et al. [50,97] for normal incidence on surfaces of different target materials such as Au and SiO_2. The X-rays emitted in flight by these ions were observed with intrinsic germanium detectors of 200 mm area and 180 eV resolution at 6 keV. The K_α- lines consist of a complex array of KL^n satellite lines corresponding to all the transitions of an L-electron to the K-shell in the presence of any number of L-spectator electrons. These satellites cannot be separated with a Si(Li) or germanium detector, but the mean energy of the measured line gives the mean number of L-electrons present at the time of decay (Tables 1 and 2, [50]). This has been verified and demonstrated [91,169] for Ar^{17+} and Ar^{18+} by comparing the same spectra recorded with a Si(Li) detector with those measured using a crystal spectrometer. It is noted that the Ar K X-ray spectrum in Fig. 7 for Ar 17+ ions, following impact on a Be target, has been measured using a micro-calorimeter detector [37]. It was demonstrated with that measurement that nearly the same resolution as with a crystal spectrometer can be achieved, while the detection efficiency was enhanced by orders of magnitude.

As shown in Fig. 7 and Table 2, the energy of the K_α-line from Fe^{25+} ions is

Table 1
Experimental and theoretical values for KL^n satellite lines in Fe^{q+} and Kr^{q+} ions [50]

Line	Fe^{25+}	Fe^{26+}	Kr^{35+}	Kr^{36+}
Experimental energy (eV)				
$K\alpha^s$	6555	6535	12,935.5	12,917.4
$K\alpha^h$		6867		13,389
Line	Fe		Kr	
Theoretical energy (eV)				
$K\alpha_2^s$ neutral	6392	$K^1L^8M^x = 6397.5$	12,605	$K^1L^8M^x = 12,631$
$K\alpha_1^s$ neutral	6404		12,657	
$K\alpha_2^h$ neutral	6558	$K^0L^8M^x = 6668$	12,990	$K^0L^8M^x = 13,018$
$K\alpha_1^h$ neutral	6678		13,047	
He-like $^3P_1$	6667	$K^1L^1M^0 = 6684$	13,023	$K^1L^1M^0 = 13,068$
He-like $^1P_1$	6701		13,114	
H-like Ly-α_2	6952.5	$K^0L^1M^0 = 6965$	13,431	$K^0L^1M^0 = 13,483$
H-like Ly-α_1	6971.2		13,509	

Table 2
Mean number of L-spectator electrons and K_α, K_β, and K_γ relative line intensities (corrected for fluorescence yields and number of L-spectator electrons during hyper-satellite cascades) [50]

Ions	Ar^{17+}	Fe^{25+}	Kr^{35+}
$K\alpha L^{(x)}$	$K\alpha L^{(5)}$	$K\alpha L^{(4.2)}$	$K\alpha L^{(2.7)}$
$I(K\beta)/I(K\alpha)$	0.3	0.38	0.42
		(No. e^-M > No. e^-L)	(No. e^-M > No. e^-L)
			(No. e^-N > No. e^-L)
$I(K\gamma)/I(K\alpha)$			
Ions	Ar^{18+}	Fe^{26+}	Kr^{36+}
$K\alpha_{sat}L^{(x)}$	$K\alpha K^{(5.4)}$	$K\alpha L^{(5.3)}$	$K\alpha L^{(3.2)}$
$K\alpha_{hypersat}L^{(x)}$	$K\alpha L^{(3.8)}$	$K\alpha L^{(3.8)}$	$K\alpha L^{(2)}$
No. of additional Le^-	2.6	2.5	2.2

centered on the KL^4 satellite (four L-spectator electrons instead of five as observed for argon). This result is consistent with the observed shape of the K_β-line (whose KL^n components are more widely separated than for the K_α-line), which shows that most of the eight satellite lines (except maybe the last KL^8 and KL^7 transitions) are present. In the case of Kr^{35+} the K_α-line is centered on a KL^n satellite, whose mean n-value is 2.7. It appears from the K_β-spectrum presented in Fig. 7 that only the few KL^n lines are present. One of the most visible features of the Fe and Kr spectra as compared to the Ar case is the enhanced ratio of the intensities of the K_β-lines to the K_α-lines: 38 and 42% for iron and krypton, respectively (Table 2). For an equal number of p-electrons in the $n=2$ and 3 shells, the transition rates for the K_β-lines compared to the K_α-lines [50] are between 15 (six electrons in each shell: neutral atom) and 26% (one electron in each shell: hydrogenlike ion). The mean number of M-electrons (of the 3p level) is always about two times as large as the number of L-electrons. As reported earlier [50] for the case of Ar, the M-shell is then roughly closed when the L-shell is empty (a similar conclusion may also be drawn for the N-shell for $K\gamma$-lines). This means, that the ion is quickly fed with electrons to reach its equilibrium charge state.

The first result of Tables 1 and 2 is the decrease of the mean number of L-spectator electrons present at the time of the K-vacancy filling as a function of the atomic number of the ion. 5, 4.2 and 2.7 L-spectator electrons are present for argon, iron and krypton hydrogen-like ions, respectively. The ions are quasi-neutralized, i.e., have comparable L-shell filling rates for an equal number of electrons (the Auger rate, e.g. for the LMM transitions varies slowly with Z). The L-shell filling rate is, however, also faster owing to the larger number of electrons in the outermost shell for ions with larger atomic mass numbers (i.e. a factor 2 between Ar and Kr). This result shows the effect of the fast decrease of the K-shell lifetime as a function of Z (the radiative lifetime is $\tau_k \sim Z^4$), which leads to a relatively faster filling rate for the K-shell than for the L-shell for increasing atomic numbers.

The second result is obtained by comparing the numbers of L-spectator electrons, *n*, for Fe^{25+} and the first K-transition for Fe^{26+} (where two K-vacancies cause hypersatellite lines), which are found to be 4.2 for Fe^{25+} and 3.8 for Fe^{26+}. This observation can be explained by considering that the lifetime of the K-hole is about two times shorter when two K-holes are present instead of one [98]. Since the L-shell filling rate in this case is roughly the same for Fe^{26+} and Fe^{25+}, this means that the K_α-line is emitted in a shorter time for Fe^{26+} than for Fe^{25+} and then for fewer L-electrons. A similar effect is also observed with Kr^{35+} and Kr^{36+} ions ($n=2.7$ for Kr^{35+} and 1.9 for Kr^{36+}).

A third result that can be extracted from the Table 2 is the mean time for the filling of an L-vacancy, which can be deduced from the energies of the satellite and the hypersatellite lines for a given element. For the bare ionic Fe^{26+} and Kr^{36+} two K-vacancies are sequentially filled through the hyper-satellite-satellite cascade [50]. By looking at the electronic configuration of the ion at the times of the filling of the two K-holes (satellite and hyper-satellite lines), it is possible to observe separately two steps of the time evolution of the electronic configuration of the hollow atoms, using that the two lines are produced one after the other. A completely different KL^n distribution was observed, where more L-electrons are present for producing the satellite spectrum than on the hypersatellite one, which demonstrates clearly the stepwise filling of the L-shell [91,169].

The lifetimes of the states during the cascade of LMM and LNN Auger transitions filling the L-shell (KL^1-KL^2-KL^3) vary slowly [91,169]; and lifetime are of the order of 5×10^{-16} s [99]. The stepwise filling of the L-shell of the ion may be described in the same way as the decay of a radioactive series by the Bateman's equations [50]. The individual lifetimes take into account the two decay channels of any KL^n state: the filling of the K- and L-shells. From the K- to L-branching ratio and the fluorescence yields one can obtain the probability to observe, at a given time, a K_α-line with a given number of L-spectator electrons. If the K_α-line is emitted at a certain time t_1 one observes a given KL^n array of satellites, (which must be different at a decay time t_2), this KL^n array of satellites then provides some 'snapshots' of the electronic configuration of the ion at this time. When two successive K_α-lines are emitted in ions having two K-holes, one can then obtained two successive 'snapshots' of the electronic configuration at two different times. For the Ar hypersatellite and the satellite transitions Briand et al. showed [91,169], that the first (hypersatellite) K_α-transition is emitted when only few L-electrons are present ($n=3.8$), while the second transition occurs in the presence of a larger number ($n=5.4$) L-electrons. Here, corrections for variations in fluorescent yields were included [100], Table 2.

The mean number of L-electrons present at the time of the second K X-ray emission is, for argon, increased by 1.6. The increase by $+1$ stems from the fact that one L-shell electron has made a transition into the K-shell in the first K_α-transition. The time that separates the emission of the first (hypersatellite) from the second K-transition is, for the $K^1L^5M^8$ configuration, of the order of 10^{-15} s. The mean time for the filling of an L-hole, around a mean value of 5.4 L-spectator electrons, would then be $[10^{-15}\ (s)]/2.6 \approx 4 \times 10^{-16}$ s, i.e. in agreement with the theoretical estimates for the partial lifetime of the LMM (plus LNN, LNO Auger transitions). It is possible, by measuring the increase of the number of L-electrons between the filling of the first K-hole and the second one to estimate the mean time for the filling of an L-hole in a given KL^n configuration. It is found to be equal to the calculated LMM (LNN, LNO) Auger rate.

The changes of the number of L-spectator electrons during the period of time between the emission of the hyper-satellite and the satellite have been found, without any fluorescence yield corrections, to be $\Delta n = 1.5$ and 1.2 for iron and krypton, respectively. Still one electron must be added because one L-electron is lost from the L-shell in the filling of the first K-vacancy. However, the relative intensity of the eight KL^n lines has to be corrected to take into account the fluorescence yield ω of each of the KL^n states (Table 3). In the case of argon, ω varies over a large range: $0.1 < \omega < 1$ (0.1 for KL^8, 1 for KL^1). For iron and krypton, the fluorescence yields are larger: $0.3 < \omega < 1$ and $0.6 < \omega < 1$, respectively. These changes around a mean number of 5 ± 1 L-electrons (iron) and 3 ± 1 (krypton) are, however, very small for iron (~15%) and for krypton (~10%).

The mean time between the emission of the satellite and the hyper-satellite τ_K, i.e., the inverse of the total transition rate for the filling of the K-shell (K X-rays plus KLL and KLM Auger), can be estimated by using the Larkins statistical procedure [102]. It is found, by using calculated KLL transition rates and scaling the radiative rates with the Z^4 law, to be approximately 3×10^{-16} s for the KL^5 state of iron and 1.5×10^{-16} s for the KL^3 state of krypton. The experimental values for the mean time required for the filling of one L-shell hole are thus about $3 \times 10^{-16}/2.5 = 1.2 \times 10^{-16}$ s for iron and $1.5 \times 10^{-16}/2.2 = 0.7 \times 10^{-16}$ s for krypton. The experimental value of the mean filling time of one L-hole in iron and krypton is roughly equal to the LMM (plus LNN, ...) Auger partial lifetime for an ion having 16 electrons in the M- and N-shells [99], i.e. $t \approx 1.2 \times 10^{-16}$ s [50].

Table 3

Calculated average K-shell fluorescence yields for Ar [49,100], Fe, Kr, and Xe [101] using the MCDF method and detailed state fluorescence yields. Effects of relativity and Breit interaction, as well as E1 and M2 transitions are included

Line	Fluorescence yield %			
	Ar	Fe	Kr	Xe
KL^8	13	37.8	67.8	90.3
KL^7	14–15	37.8	68.0	90.4
KL^6	15–17	44.2	73.5	92.3
KL^5	18–20	46.9	75.1	92.8
KL^4	18–25	51.8	78.6	94.0
KL^3	20 ± 5	56.1	77.2	88.5
KL^2	50 ± 30	70.9	84.1	95.5
KL^1	100	100	100	100

Since the M-shell is filled roughly two or three times faster than the L-shell, it is possible to give an estimate of the mean time for the filling of the whole M-shell in the case of argon. The M-shell filling has to be roughly 8/3 of the time for the filling of an L-vacancy at the beginning of the interaction (KL^1 or KL^2 state), i.e. of the order of 10^{-15} s. At velocities of the order of 1.2×10^6 ms/1 (20 kV/q) such a filling process would occur along a mean range of 12 Å, corresponding to about three or four monolayers of target atoms. Ignoring the slower depopulation of the M-shell via LMM Auger cascades, then a mean number of about two or three electrons is captured in the M-shell. These mean numbers and the rate of capture obviously vary in time, i.e., along the ion path below the surface. It decreases with time and then charge, leading to an asymptotic number of M-electrons. For iron and krypton ions the filling rate is faster, but many more electrons have to be transferred (e.g. via side feeding) to reach the equilibrium charge state and one can expect that the full neutralization still holds along few atomic monolayers. It is noted that the atomic de-excitation times are consistent with the total ionic equilibration times found from energy loss measurements described above and are fast compared to the plasmon frequencies.

K X-ray emission studies on $Xe^{53+,54+}$ have been performed at the LLNL Super EBIT [97]. The extracted Xe^{53+} ion beam has been sent onto gold and SiO_2 targets at 8.5 keV/q initial kinetic energy. The X-rays emitted in flight by these ions have been observed with a Ge(Li) detectors and have been compared to multiconfiguration Dirac-Fock calculations. The first analysis shows that an average number of 2.5 L-shell electrons is present at the time of the K X-ray emission. Interestingly for decelerated Xe^{53+} ions (12 eV/q) it has been found that the emission of the X-rays above the surface exhibits a component of a pure He-like state. This can be attributed to a time when the ion has lost all the captured electrons but one and is in a singly excited He-like state. A preliminary analysis of the energy and relative intensity of the Lyman $\alpha, \beta, \gamma, \delta, \epsilon \ldots$ lines leads to following conclusions:

1. Below the surface the electrons are captured into the highest available states of a Xe ion inside a solid, i.e. the O, P ... shells.
2. These ions contain more than 35 excited electrons.
3. The KL^x characteristic X-ray satellite pattern is strongly peaked on the KL^2 line in agreement with the expected Z^{-4} law of variation of the K-shell lifetime.
4. Similar spectra have been observed for the gold and silicon dioxide targets.

3.4.2. L-shell X-ray emission

The L and M X-ray spectra as a function of the incident charge state has been measured for highly charged Xe ion impact [2,94] with a Si (Li) detector perpendicular to the beam axis. We discuss the ion neutralization dynamics for slow (7 keV/q) highly charged Xe ions incident on a Cu surface at 45° incidence, where the number of L-shell vacancies in the incident Xe^{q+} ($q = 44$–48) projectile is systematically changed. Here, $q = 44+$ represents the closed shell $1\,s^2 2\,s^2 2p^6$

ground-state configuration of Xe and the other charge states are characterized by open L-shell configurations differing in the incident number of 2p holes. The theoretical method used to predict radiative-transition energies and transition probabilities for Xe ions with different numbers of L-shell vacancies is presented elsewhere [94,103].

The Xe^{44+} spectrum consists only of lower-energy M X-ray peaks due to the missing L-vacancy states of the incoming projectile ion. No additional L-shell vacancies are produced during the impact of the ion on the surface. The spectra resulting from Xe^{45+} to Xe^{48+} initial projectiles show higher-energy L X-ray-line structures, which arise predominantly from electric-dipole transitions into empty 2p states. In accordance with the increasing number of 2p vacancies the measured L-line energy positions shift towards higher energies with increased charge state q. Due to many satellite-line groups and limited energy resolution of our Si (Li) detector the observed line intensities are averaged over several closely spaced line groups. The range of the calculated 2p–3 d transition energies shows that the satellite groups originate from $1\ s^2 2\ s^2 2p^k$ ($k=2$–5) initial inner-hole-state configurations. These include about 350 possible satellite lines with center energies varying from 4053 to 5166 eV for Xe^{45+} and 4 × 350 satellite lines for Xe^{48+} projectiles with a total energy variation of about 4053 to 4955 eV.

Even though the maximum of the measured structures lies in the energy range predicted for the satellite group there is a tail of the intensity to higher energy with a shoulder at about 4.7 keV. Additionally one observes a group of lines at around 5.6–6 keV, which originates mainly from 4 d–2p transitions.

From the analysis it was found that the main intensity of the high-energy peaks in the L-line group stems from transitions associated with 4 d states. Some intensity from 5 d and 6 d states is observed. In fact, the most significant radiative transitions observed may arise from 4f states. The 4f is most probably populated by direct capture into $n=4$. This in turn may lead to a strong excitation of $n=3$ levels via cascade mechanisms [94,104] when the ions have already penetrated into the solid. Considering the lower detection efficiency for the M X-rays (~factor of 2) compared to the L X-rays it is obvious that the M intensities are actually larger than the L-intensities. From the comparison of the observed line energies and the theoretical calculations it is found that the main peak in the M X-ray group arise from a population of $n=4$ states. Moreover, the peak on the high-energy side of the $n=4$ structure is due to $n>5$ states. By comparing the maxima for the 4–3 ($n=4$ to $n=3$) transition for Xe^{45+} and Xe^{48+} a shift of approximately 224 eV is observed. From a comparison of the observed M-spectra and the predicted energy values it was concluded that a large fraction of initial $2p^k$ cores states have survived when the 4–3 radiative de-excitation occurs.

Following the over-barrier model one finds that the neutralization process starts at a critical distance $R_c \sim 130$ Å for Xe^{45+}. The highest n-states populated by electron transfer from the copper surface has been estimated by taking the binding energies, the image-charge potential and the work function of Cu into account. This gives a maximum value of approximately $n=43$. On the way into the surface, capture will occur to somewhat lower n-values due to the change of screening and energy-level shifts owing to the increased image charge. One expects a 'band' of Rydberg levels to be populated between about $n=20$ and 40 during the approach to the surface. No information exists about the distribution of electrons among those n manifolds. The situation is further complicated due to Stark mixing near the surface. In this connection, we note that no clear signature of the direct decay of highly excited hollow atom states has been found in the measured X-ray spectra. However, some direct, fast radiative transitions from superexcited states with $n \approx 20$–40 may weakly contribute to the high-energy tail above the main M and L X-ray structures. However, these features cannot be resolved with present energy resolution and low beam intensity. In conclusion, one finds that the direct population of the $n=3$, 4, and 5 levels occurs in the solid where some fraction of the $n=3$ population comes from cascading via $n=4$ or even $n=5$.

It is assumed that the n-levels are populated by a pronounced side-feeding mechanism. For the present projectile beam energy and ion beam-target geometry, the approach velocity is about 0.22 a.u. corresponding to 7 Å/fs, which means that the time interval between the first capture events and the ions striking the surface is about 4×10^{-15} s. This interaction time is much too short for substantial cascading to lower states. Hence, the highly excited states consisting of a core of ($1s^2 2s^2 2p^k$) inner-shell configuration and a band of electrons in $n \approx 20$–40 ('hollow atoms') survive until the ions hit the surface. After the ion has penetrated into the solid, it experiences close binary collisions with Cu target atoms where resonance charge transfer may occur. In this way, the M-shell can be

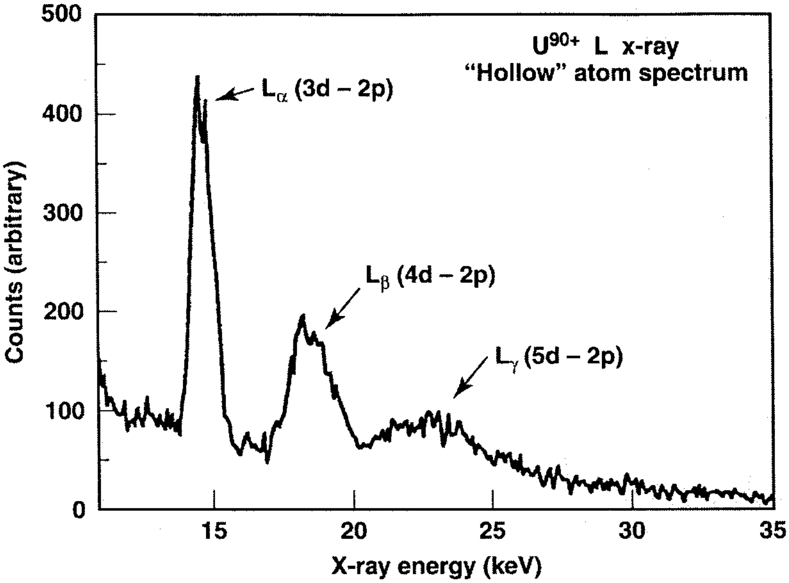

Fig. 10. L X-ray emission spectrum from the radiative de-excitation of 450 keV U^{90+} ions incident on a Au target.

partially filled by direct electron capture since it is near resonance with the Cu L-shell and the critical instance can be estimated to be 0.25 a.u. On the other hand, the 2p vacancies of the core survive because the Xe L-shell with binding energies around 7961–8719 eV is not resonant with any atomic state in Cu making cross sections for this channel prohibitively small.

Recently, L-shell X-ray emission spectra following 7 keV/q $U^{86\pm\text{-}90+}$ impact on a Au target have been measured at the Super EBIT; Fig. 10 shows a spectrum from U^{90+} impact. From this spectrum and comparison to the Xe spectra, an enhanced L_β and L_γ intensity and energy spread is observed. The enhanced intensity indicates the 'L-shell hollow atom' must have a substantial number of electrons in high n-states ($n > 6$). A preliminary calculation of transition energies and comparisons with observed peak energies suggests that in this case the hollow atom might contain more than 60 electrons in the outer shells.

3.4.3. M-shell X-ray emission

Uranium M X-rays for U^{q+}, $62 \leq q \leq 73$ impact on a Be surface have been studied for impact energies of 7 keV/q [95]. The energies for the transitions into the M-shell were calculated using Dirac–Hartree–Slater model [105]. When the ions start to penetrate into the bulk, most of the high n-electrons are stripped off. Closer collisions with lattice atoms transfer electrons into lower n-states, with $n \cong 8$–10. These electron cascades into inner-shell vacancies, giving rise to M X-rays if M-vacancies are available. In calculating the transition energies, electrons were statistically distributed in the $n = 4$ to $n = 6$ states for charge states from $q = 15$ to $q = 40$. As a result, predicted energies are distributed over energy bands. A comparison of the measured spectra with the predicted transition energies indicates that most of the observed intensity results from M X-rays. As predicted, the centroid of the main peak shifts to higher energy as the initial charge of the projectile is increased. The most interesting feature of the data is the observation of significant M X-ray emission from U-ions incident on the Be surface with no M-vacancies ($q \leq 64$) initially in the ion. An explanation for the observation of the anomalous M X-ray emission is the possibility of direct collisional excitation or ionization of M-shell electrons. One finds that this process has an extremely low probability. The velocity of the ions is approximately 0.25 a.u. while the minimum excitation energy for an M-shell electron is more than 220 a.u. For a similar reason one could also exclude molecular orbital promotion in this very asymmetric target-projectile system. Neither can metastable states in the incoming ions explain the observed spectra, since it is known that very few ions in metastable states are produced from an electron beam ion source, such as EBIT.

The integrated intensity of the main M X-ray peak normalized to the number of incoming ions shows that the M X-ray yield increases monotonically with charge state, but with a different slope above and below $q = 64$. The approximately linear relationship of the X-ray yield with charge state for $q \geq 65$ is the expected variation as the number of M-vacancies in the ion increases. The slope for $q \leq 64$, however, seems to reflect the number of N-shell vacancies, indicating a mechanism for creating M-shell vacancies using N-shell vacancies.

A new mechanism of *internal dielectronic excitation* (IDE) facilitating the production of M-shell vacancies during relaxation of hollow atoms was proposed by Knapp et al. [106] in collaboration with Schuch et al. [95]. If a 3lnl′ state is energetically degenerate with a doubly-excited 4l4 l′ state, then a resonant transition between the states is possible. The resulting intermediate 4l4l′ state may decay either radiatively to a 3l4 l′ state, or nonradiatively back to 3lnl′ state. In the former case, an M X-ray is observed. The steps leading to M X-ray emission by this mechanism are shown in [95]. Given the presence of such an energy degeneracy, the rate for formation of the intermediate state with an M-shell vacancy is expected to be quite large compared to other decay rates in the hollow atom. In the system studied here, the formation of 4l5 l′ or higher intermediate state is not energetically allowed. It is noted that the L-shell excitation via the IDE process is energetically not possible (see Xe case).

The energy degeneracy condition requires that some electrons in a high-*n* state have a transition to the N-shell with an energy that exactly corresponds to a transition energy between the M- and N-shells. While this condition might at first seem difficult to satisfy, the large number of captured electrons cascading through the closely-spaced high-*n* states, together with the large number of satellites for both the M–N transitions and the high-*n* states, make it possible. This was shown from binding and transition energies calculated using the Dirac–Hartree–Slater model [105].

In order to generalize the IDE effect, other projectile–target combinations have been studied. The M X-ray emitted from Bi^{q+} ions following the interaction with gold surfaces, for which the projectile is not expected to have initial M-vacancies (q is smaller than 55) have been measured [107]. Here the use of a gold rather than a Be target makes vacancy production by molecular-orbital promotion possible. In the Bi ions with charge states in the range of $q = 50$–71 were accelerated to energies of $q \times (7\ \mathrm{keV})$ and were directed to a gold target. X-rays were observed with a Si(Li) detector. Two distinct energy ranges of X-rays are observed, one of these in the range of 750–2000 eV and the other between 2500 and 6000 eV. Both ranges shift to higher energies with increasing incident ion charge state. The lower energy group, which dominates the spectra for lower incident charge states, is in the range expected for the filling of vacancies in the N-shell. The higher energy group, which predominates for the higher incident charge states, is in the range that might be expected from the filling of M-shell vacancies. In order to determine the two ranges of lines, transition energies were calculated with Froese–Fischer's Hartree–Fock program [108] and outer electrons were removed sequentially. The analysis did establish peaks between 750 and 2000 as having their probable origin in the filling of the N-shell and those between 2500 and 6000 eV, to the filling of the M-shell.

No evidence is observed for decay into these shells directly from high Rydberg states, the continuum or the Fermi level of the gold. Evidence is seen in the spectra with $q = 52$ and $q = 55$ for M X-rays being emitted from ions that enter the collision without the requisite M-vacancies. An integration of the spectral intensities between 2500 and 6000 eV and normalization to the number of incident ions gives a plot of the relative X-ray production correction versus charge q (Fig. 11). The step of the cross section at charge 65 indicates a shell effect for the filling of the M-shell. The cross section behavior provides possible evidence for the existence of the internal dielectronic process, such as that proposed above for the uranium case. However, for this heavy projectile-target combination, the production of M-vacancies through molecular promotions cannot be excluded.

3.4.4. Soft X-ray emission studies

Soft X-ray emission (< 1 keV) studies, following slow highly charged ion impact ($Z < 18$, $q < 17$) on conductor surfaces, have been performed by various groups [109–112].

Andrä et al. [109] reported high resolution Ne K X-ray measurements from Ne^{9+}-ions (140 to 35 keV) incident on a Ta surface. The vertical velocity has been varied via the angle of incidence. Changing from the large to the low impact energy resulted in a dramatic change of the resolved satellite line intensities, which was interpreted in terms of different contributions from the resonant neutralization and autoionization at different velocities.

Briand et al. [112] reported K X-ray measurements following 10 keV/q N, O and Ne hydrogenlike ion impact on C and Si surfaces at normal incidence. The analysis of the X-ray emission from below the surface showed that the electron promotion mechanism, represents only a small part of the interactions occurring at the first atomic layer. Neutralization takes place, below the surface, mainly via Auger neutralization.

Ninomiya et al. [111] reported soft X-ray measurements in collisions of slow Ar^{q+} ions with a C target. Ar L X-rays corresponding to the filling of initial L-shell holes were analyzed and it was found that the L-shell holes were filled

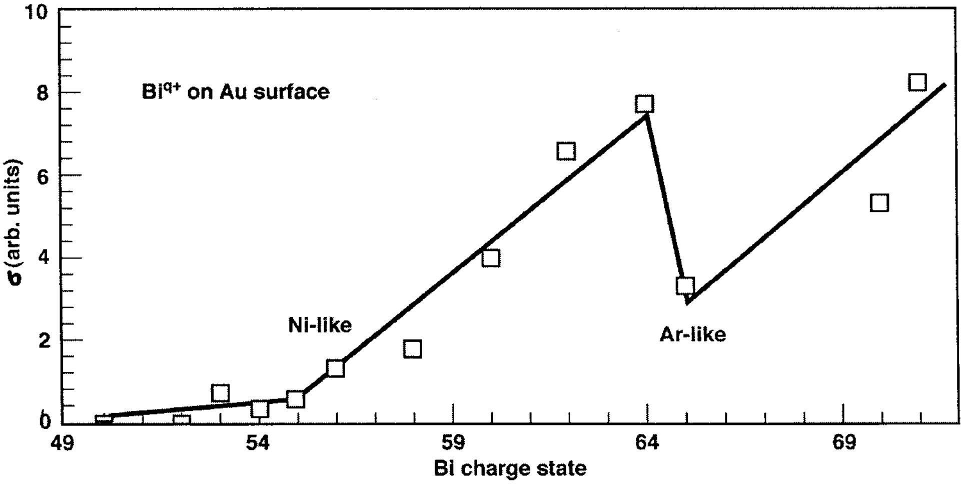

Fig. 11. Cross section (arb. units) for Bi M X-ray emission versus Bi charge states.

Table 4
Compilation of sputter yield data for multiply and highly charged ions. The column $S = S(q)$ indicates whether or not a charge state dependency of the sputtering yield was observed

Target material	Target specification	$S = S(q)$	Maximum ion charge	Model of electronic sputtering	Reference
NaCl	Insulator (alkali halide)	Yes	Xe^{25+}	Defect mediation	[114]
CsI	Insulator (alkali halide)	Small	Ar^{11+}	Defect mediation	[113]
LiF	Insulator (alkali halide)	Yes	Xe^{27+}	Defect mediation	[24,25,165]
$LiNbO_3$	Insulator (oxide)	Small	Ar^{11+}	N/A	[113]
SiO_2	Insulator (oxide)	Yes	Xe^{25+}	Defect mediation	[25]
UO_2	Insulator (oxide)	Yes	Th^{70+}	Coulomb explosion	[10]
Si	Semiconductor	No	Ar^{9+}	N/A	[114,119]
GaAs (100)	Semiconductor	Yes	Ar^{9+}	Coulomb explosion	[115,172]
GaAs	Semiconductor	No	Ar^{9+}	Defect mediation	[25,114]
GaAs (100)	Semiconductor	Yes	Th^{70+}	Structural instability	[30]
Au	Metal	No	Ar^{9+}, Ar^{11+}	N/A	[113,114]

stepwise primarily via 3 s–2p transitions; similar results were obtained for a Be target. Ninomiya et al. [110] also reported on N K X-ray measurements following passage of 2.1 keV/u N^{6+} ions through a thin microcapillary foil. The X-rays were measured in coincidence with the exit charge state. Ions with a K-hole, but with several electrons in outer shells, were successfully extracted into the vacuum. It was found that a considerable fraction of extracted hollow ions had extremely long lifetimes of the order of ns. Stabilization of hollow atoms in vacuum was attributed to spin-aligned electrons in outer shells.

3.5. Sputtering of surface atoms

The question of mechanisms for sputtering and secondary ion emission in the interaction of SHCI with solids has been subject of controversial discussions following early claims of strong enhancement of emission yields as a function of projectile charge state or potential energy (see discussion in [1] and [113]). Only recently, total sputtering yield and secondary ion yield measurements have become available for insulators, semiconductors and metals and for SHCI with charge states up to Th^{70+} [10,30]. In the following, we will review results from total sputter yield and secondary ion measurements with the focus on elucidation of various sputtering mechanisms such as defect mediated sputtering, Coulomb

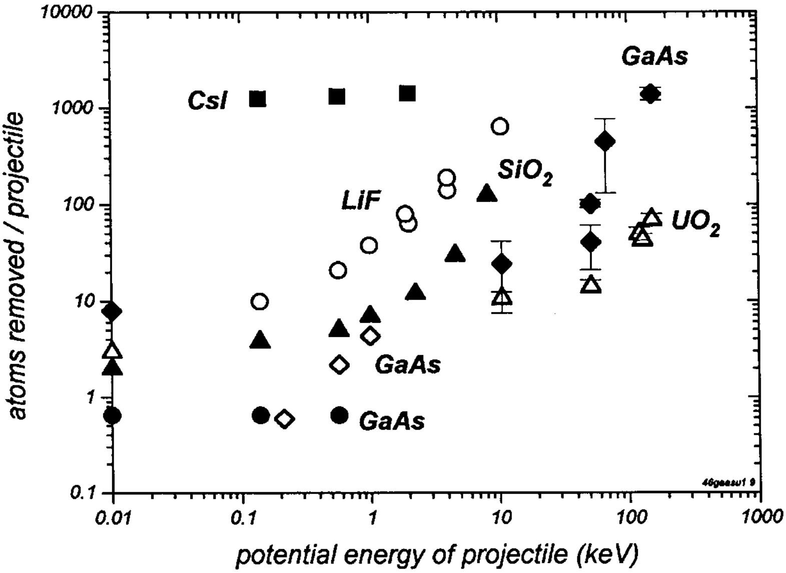

Fig. 12. Total sputtering yields for CsI, solid squares, [113]; LiF, open circles, [25]; SiO_2, solid triangles, [25]; GaAs, solid circles, [114], open diamonds [115,172], solid diamonds [30]; and UO_2 open triangles, [10] vs potential energy of projectile. Kinetic energies of projectiles were constant within each data set but varied in measurements by different groups.

explosions and intense electronic excitations. After presentation of experimental results, we will discuss recent developments in theory of electronic sputtering by SHCI in Section 4.

3.5.1. Total sputter yields

In extended measurements with the microbalance technique, Sporn et al. [25] and Varga et al. [114] have measured sputtering yields for a range of materials including insulators, semiconductors and pure metals (see Table 4 and Fig. 12) for very slow projectiles up to Ar^{14+} and Xe^{27+}. In covering these materials classes, they provided a rather complete data set on the base of which the question of microscopic sputtering mechanisms can be addressed for the relatively low charge states available with ECR sources. Defect mediated sputtering, a mechanism well known from a wealth of *desorption induced by electronic transitions* (DIET) studies, could be identified for sputtering of LiF and SiO_2. Very low secondary ion yields and an absence of potential sputtering for materials were electronic defects (e.g. self trapped excitons or holes) can not be stabilized, such as GaAs or MgO, clearly ruled out Coulomb explosions as an important mechanism in the charge state regime below 27+ for xenon.

Results for GaAs are controversial. In measurements using a quadruple mass spectrometer, Mochiji et al. [115,172] and Itabashi et al. [116] reported a charge state dependency of total sputtering yields for the same projectiles (i.e. Ar^{9+}, $E_{kin} = 500$ eV), as used by Varga et al. [114]. Next to the different techniques for determination of total ablation yields, targets differed in that Varga et al. [114] used a polycrystalline GaAs film formed by molecular beam epitaxy, while Mochiji et al. [115,172] used crystalline GaAs (100). Mochiji et al. [115,172] interpret their findings in terms of the early, phenomenological Coulomb explosion model [117,125].

Using the catcher technique, Schenkel et al. [10,30] determined sputter yields for GaAs(100) and uranium oxide interacting with SHCI like Xe^{44+} and Th^{70+}. Sputtering signatures for the heavy metal oxide, i.e., high secondary ion yields and strong cluster ion emission point towards contributions from Coulomb explosions. For GaAs interacting with Th^{70+} ($v = 30\ v_{Bohr}$) some 1400 atoms are removed per incident SHCI. Here, relatively low ionization probabilities and the absence of significant cluster ion emission point beyond Coulomb explosions and defect mediated sputtering towards effects of intense, ultrafast electronic excitations. Similar high ablation yields have been reported before, but only for very radiation soft alkali halides, such as CsI [113] and very recently for pure metals interacting with heavy cluster ions [118]. We will discuss the differentiation of competing sputtering mechanisms at the end of Section 4.

3.5.2. Secondary ion emission

Studies of secondary ion emission as a function of projectile charge state and impact velocity give important information on sputtering mechanisms and lay the foundation for new surface analysis techniques such as HCI based secondary ion mass spectrometry and emission microscopy (see Sections 5.1 and 5.2). Ionization processes in low energy ion irradiation of solid surfaces have recently been reviewed by Gnaser [120].

Potential sputtering of protons from fullerene targets by slow ($v \sim 0.01\ v_{\text{Bohr}}$) argon ions ($q \leq 16+$) was reported by Kakutani et al. [121,173]. Secondary ions from fullerenes were not observed. Proton yields were found to follow a power law dependency on projectile charge, $Y(\mathrm{H}^+) \sim q^n$. Values for the exponent, n, were found to be about 4–5, significantly higher than in a previously found cubic charge dependency for proton desorption from insulating organic (phenylalanine) and inorganic (CsI and $\mathrm{SiO_2}$) targets by Ar^{q+} with $q = 1+$ to $11+$ and at $v = 0.14\ v_{\text{Bohr}}$ [39,122]. The very strong increase of proton yields as a function of projectile charge state was reproduced by Burgdörfer and Yamazaki [123] in the framework of a pre-impact desorption model were breaking of the C–H bond in the course of above surface, potential electron emission results in a localized Coulomb explosion.

Secondary ion emission from thin carbon foils was reported for impact of highly charged xenon ions by Terasawa et al. [124] and for charge states up to 70+ for thorium ions by Schenkel et al. [39]. Here, high yields of protons, positive and negative carbon and hydrocarbon ions were interpreted in terms of a phenomenological Coulomb explosion model [125].

Observations of secondary ion yield increases by two to three orders of magnitude as a function of projectile charge state have stimulated studies of secondary ion emission for a number of insulating and conductive targets such as

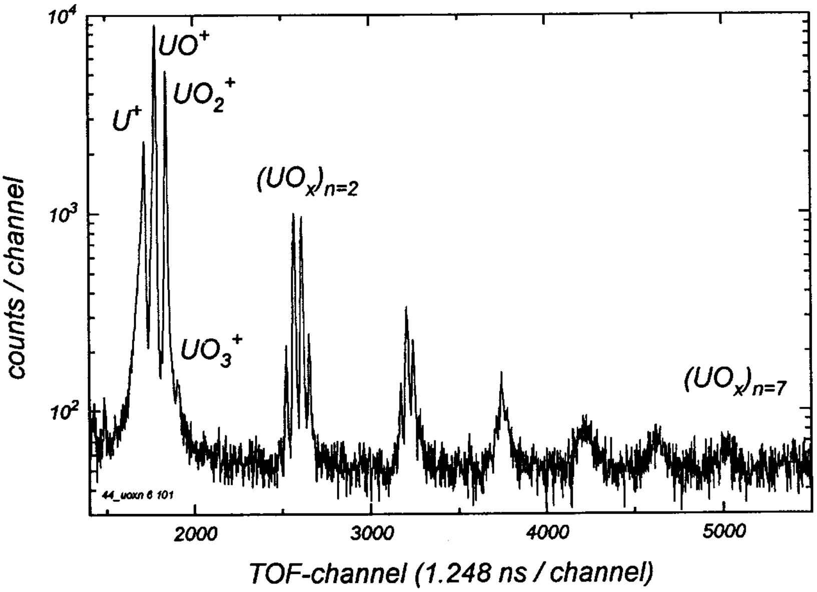

Fig. 13. TOF-SIMS spectrum of positive secondary ions emitted from uranium oxide following impact of Au^{69+} ions at 220.8 keV [10].

SiO_2 films on Si [19,126,127,164], hydrocarbon films on gold [19,164], self assembled alkyl monolayers on silicon (111) [128], uranium oxide [10], lithium fluoride [24,165], gallium arsenide [30], silicon [33,126,129], highly-oriented pyrolytic graphite [19,33,164], as well as a number of metals (Al, Ni, Ag, Cu) [129] and some complex organic and inorganic molecular solids such as DNA [130], gramicidin S [34] and fullerenes [127].

While characteristics of secondary ion emission reveal important information on sputtering and desorption mechanisms, knowledge of ionization probabilities and thus total sputtering yields is mandatory for understanding of the response of solids to electronic excitation by SHCI. In the following, we will discuss in more detail results for gallium arsenide and uranium oxide, two materials for which both secondary ion yields and total ablation rates have been determined.

3.5.2.1. Positive secondary ion yields from GaAs and UO_2. An example of a TOF-SIMS spectrum of positive secondary ions emitted from uranium oxide interacting with Au^{69+} ions is given in Fig. 13 [10].

High yields of heavy molecular clusters are detected with up to 7 repeat units of $(UO_x)^+$, $x=0, 1, 2, 3$. Similar cluster emission has been observed for SiO_2 targets interacting with SHCI [19,127,164]. In contrast, positive secondary ion spectra from GaAs (100) were dominated by Ga^+ and few As^+ ions with only negligible presence of cluster ions ($\ll 10^{-3}$ counts per projectile). The dependency of positive secondary ion production on projectile charge, q, is shown in Fig. 14.

For uranium oxide, projectiles were $Xe^{17,19,20,27,31,38,44,48,52+}$ (open triangles)

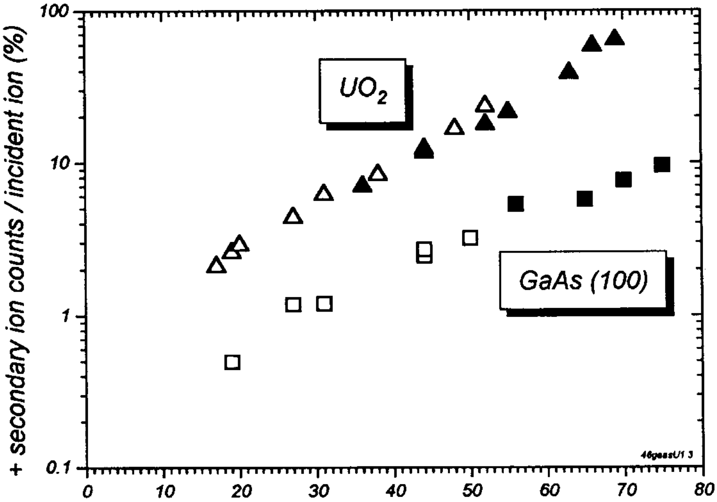

Fig. 14. Positive secondary ion production from uranium oxide (triangles) and GaAs (100) (squares) as a function of projectile charge state, q.

and $Au^{36,44,52,55,63,66,69+}$ (solid triangles). The impact velocity was kept constant at $0.2 \times v_{Bohr}$. Uranium ion yields include contributions from all uranium oxide clusters. Projectiles and impact velocities for GaAs (squares) were: Xe^{19+} ($v = 0.18\ v_{Bohr}$), Xe^{27+} ($v = 0.29\ v_{Bohr}$), Xe^{31+} ($v = 0.23\ v_{Bohr}$), Xe^{44+} ($v = 0.28\ v_{Bohr}$), Xe^{50+} ($v = 0.3\ v_{Bohr}$), Th^{56+} ($v = 0.28\ v_{Bohr}$), Th^{65+} ($v = 0.26\ v_{Bohr}$), Th^{70+} ($v = 0.27\ v_{Bohr}$) and Th^{75+} ($v = 0.28\ v_{Bohr}$). Up to 0.6 U^+ ions were detected per Th^{70+} projectile. Yields from GaAs are almost an order of magnitude lower. Data shown are positive secondary ion counts detected per incident projectile. Total sputtering yields from the semiconducting target exceed those from the heavy metal oxide by a factor 20. Conversely, positive secondary ion yields from the metal oxide exceed those from the semiconductor by almost a factor of 10.

3.5.2.2. Ionization probabilities. Having measured both total sputtering and secondary ion yields, Schenkel et al. [10,30] determined the ionization probabilities for positive secondary ions. The ionization probability, α, is defined as the number of positively charged secondary ions emitted per sputtered atom. The charge dependency of α (Fig. 15) follows opposite trends for the two materials. Data points at $q = 1$ give estimates of ionization probabilities for collisional sputtering [131,132]. These values are upper limits calculated from secondary ion yields for xenon projectiles with the lowest charge state divided by total yields calculated with SRIM [131].

For uranium oxide, α increases by about an order of magnitude from the

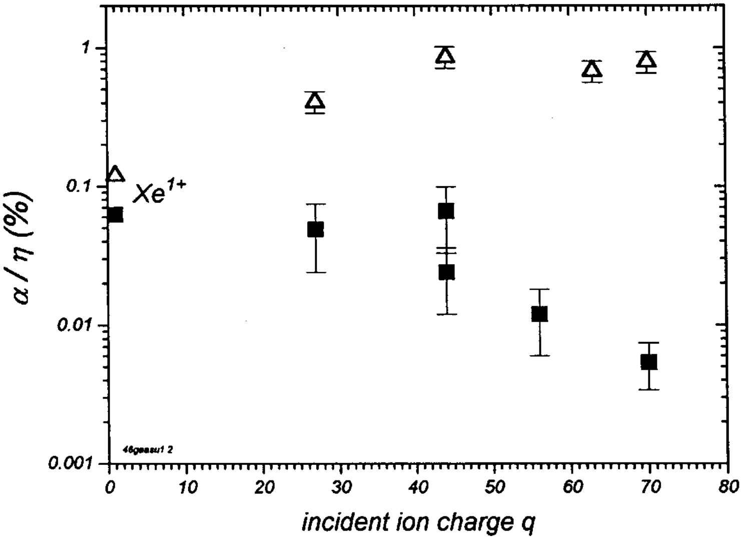

Fig. 15. Ionization probability, α, for positive secondary ions from uranium oxide (triangles) and GaAs (100) (squares) as a function of projectile charge state, q. α is normalized to the detection efficiency of the TOF-SIMS spectrometer, η, of 0.1–0.15.

estimated collisional limit. In contrast, α for GaAs(100) decreases by over an order of magnitude as a function of q.

3.5.2.3. Cluster ion yields. A notable difference in secondary ion spectra from the two materials studied here is in the emission of charged clusters. While absent for GaAs, high yields of heavy clusters were observed for the heavy metal oxide. In Fig. 16, we show the increase of $(UO_x)_1^+$ and $(UO_x)_2^+$, $x=0$, 1, 2, 3, as a function of q. We included least square fits of ion yields to simple power laws, $Y \sim q^n$, with different coefficients. It is apparent that the increase in q is much more pronounced for the cluster ions than for uranium-oxide molecules. The very steep increase ($\sim q^6$) for $q > 35$ points towards a threshold and the onset of a new sputtering mechanism once a critical excitation strength is exceeded.

3.5.2.4. Positive secondary ion yields vs impact energy. The dependency of secondary particle emission on the kinetic energy of projectiles gives insight into contributions from electronic (inelastic) vs nuclear (elastic) processes in sputtering of materials by singly charged ions. For slow, highly charged ions, the influence of kinetic energy has been shown to be small [10,19]. This can be expected since all the potential energy, but only a small fraction of the kinetic energy of SHCI is deposited near the target surface [60,167]. Non-linear increases of total sputtering yields were observed over 20 years ago in self-sputtering of gold. Heavy projectiles impinging on heavy targets set most of the target atoms along their path into motion and create what was called an elastic collision spike [133,134,174–176].

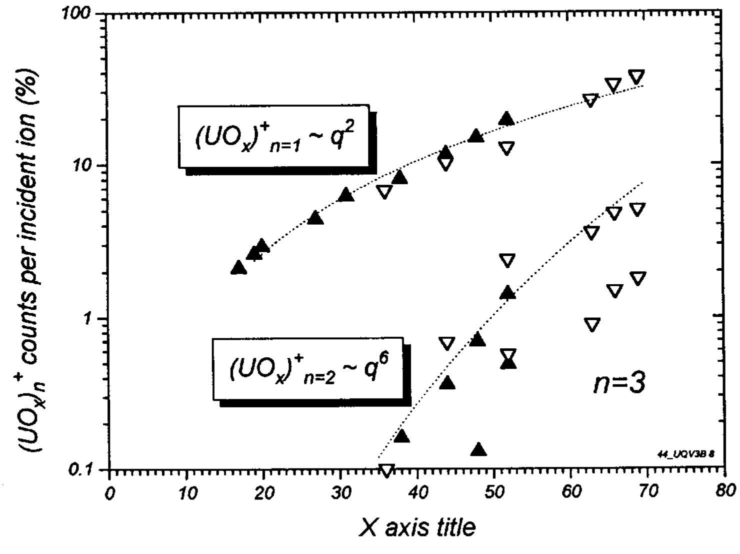

Fig. 16. Yields of $(UO_x)_1^+$ and $(UO_x)_2^+$ cluster ions from uranium oxide as a function of projectile charge, q. The kinetic energy of projectiles was 195 keV.

These spikes manifest themselves in a characteristic energy dependency of sputtered neutral and ion yields [118,134,174–176].

Measurements of secondary ion yields from uranium oxide as a function of kinetic energy for Xe^{27+}, Xe^{44+}, Au^{63+} and Au^{69+} were presented in Ref. [10]. Ion yields varied only very weakly for xenon projectiles when the impact energy is increased from 20 to 500 keV. The yield dependence for Au^{63+} displayed some structure with a weak maximum. However, data for Au^{69+} showed a pronounced maximum at ~220 keV. An energy value consistent with observations in elastic collision spike sputtering [118,134,174–176] where the maximum sputter yield is achieved at energies slightly below the projectile energy corresponding to the nuclear stopping power maximum. The latter is reached at a kinetic energy of ~600 keV for singly charged gold ions in uranium oxide [131]. The finding of a more pronounced maximum in secondary ion emission for a more highly charged projectile demonstrates the critical interplay of projectile momentum and charge. For Au^{63+} ($E_{\text{pot}} = 122.3$ keV), the combination of high charge and momentum yields a weak but significant increase in secondary ion emission at elastic collision spike energies. For Au^{69+} ($E_{\text{pot}} = 168.6$ keV) the additional electronic excitation energy creates a condition above a critical level in both charge and momentum. Consequently, electronic sputtering through charge neutralization and elastic collision spikes combine synergistically. Increasing or decreasing the impact energy decreases momentum transfer below critical values for spike formation and yields drop similarly as observed in pure elastic spike sputtering. While conditions for

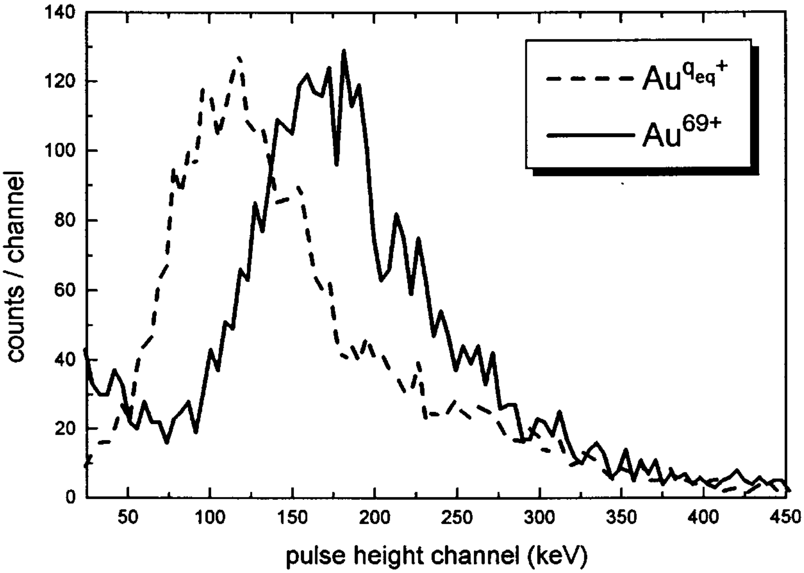

Fig. 17. Pulse height distributions from an ion implanted silicon detector for gold ions in charge state equilibrium ($q_{\text{eq}} \approx 1.6+$) and Au^{69+} ions with kinetic energies of 447 keV.

elastic collision spikes are lost, intense electronic excitation keeps secondary emission levels high. For gallium arsenide, secondary ion yields varied only insignificantly when the kinetic energy of Th^{70+}-ions was varied between 196 and 525 keV. No evidence for a synergistic interplay of electronic excitation and elastic collision spikes was found for this lighter (lower Z) semiconductor.

3.6. Deposition of potential energy in solids

In Fig. 17 we show pulse height distributions from a passivated and ion implanted silicon detector responding to the impact of gold ions in charge state equilibrium ($\mathrm{Au}^{q_{\mathrm{eq}}^{+}}$, $q_{\mathrm{eq}} \approx 1.6+$) and Au^{69+} ($E_{\mathrm{pot}} = 168.6$ keV) were the kinetic energies were kept constant at 447 keV. Projectiles in charge-state equilibrium were prepared by transmission of HCI through thin carbon foils. The foil bias was adjusted to compensate for energy loss in the foil so that highly charged and charge-state equilibrated projectiles reached the detector surface with the same kinetic energy. The pulse of collected charge in the PIPS detector stems from low energy electrons that have diffused through the contact layer into the depletion region and from electron-hole pairs created in the depletion region by energetic photons, electrons and the charge-state equilibrated projectile. The mean pulse height in Fig. 17 is significantly increased due to deposition of potential energy by Au^{69+}. These first results indicate that the pulse height increase represents about 35% or 60 keV of the available potential energy [135]. The potential energy is traced in the depletion region of the PIPS, i.e., over 50 nm deep inside the solid. In contrast, only about 10% of the potential energy has so far been accounted for in measurements of emitted secondary particles.

4. Theoretical models of sputtering by SHCI

A theory of electronic sputtering of materials by SHCI must describe microscopic mechanisms for the transfer of projectile potential energy, or electronic excitation energy, into the motion of sputtered particles. Total yield data have been interpreted, in the past, by either Coulomb explosions [115,125,172] or defect mediated sputtering mechanisms [25,114,136]. In the following, we will discuss models of electronic sputtering in light of these result.

4.1. Defect mediated desorption

The defect mediated desorption model considers formation of localized defects, such as *self-trapped electrons* (STE) or *self-trapped holes* (STH), in response to valence band excitations in materials like alkali halides and $\mathrm{SiO_2}$. Sputtering of mostly neutral atoms follows the diffusion of defects to the surface. A yield of 300 LiF molecules was observed for very slow (0.6 keV) Xe^{27+} projectiles [25]. The absence of a charge state dependent increase of sputtering yields in materials where no STE are known to be formed, like GaA (100) [137,138] and MgO, served as strong evidence for the validity of the defect mediated sputtering model [25,114].

Results for GaAs and uranium oxide interacting with Th^{70+} demonstrate that defect mediated sputtering is not the only mechanism of electronic sputtering by SHCI. The defect model applies for electronic sputtering of materials where stable electronic defects can be formed. Its application is indicated for conditions of relatively low excitation densities where the materials response is dominated by the decay of individual defects.

4.2. Coulomb explosion sputtering

In the Coulomb explosion model, target atoms receive kinetic energy in the surface equivalent of an ion explosion spike [117,125,139–142,177]. A surface domain with high ionization density is formed in the course of electron emission during relaxation of SHCI. Several hundred, mostly low energy (<20 eV) electrons are emitted from metals and insulators by SHCI like Xe^{44+} and Au^{69+} [2,19]. In insulators and poor conductors, charge neutrality can not be reestablished on the time scale of several picoseconds, i.e., before ionized target atoms are repelled from each other in a Coulomb explosion. The rapid expansion of target material is thought to send a shock wave into the material. The intersection of the latter with the surface can lead to the desorption of neutral and charged molecules and clusters [19,141,142,164].

The main argument against the Coulomb explosion mechanisms questions whether hole lifetimes even in insulators are sufficiently long to prevent re-neutralization of the charged domain before the lattice can respond [136]. Mochiji et al. have argued that lifetimes are significantly longer when many holes are generated at close vicinity to each other [115,172]. To our knowledge no direct measurements of hole lifetimes and densities of hole excitation are currently available for SHCI–solid interactions.

The degree of ionization of secondary ions is a signature of the sputtering mechanism. In defect mediated sputtering, ionization probabilities, α, are small, typically $\leq 10^{-3}$ [24,25,165]. Coulomb explosions should be accompanied by emission of high yields of positive secondary ions [139,141,143,177]. The observation of an increase of α as a function of projectile charge, q, for the heavy metal oxide is consistent with a Coulomb explosion mechanism, while the opposite trend for GaAs points to a different sputtering mechanism. At the given transmission of our TOF-spectrometer, ion fractions are $\sim$5–8% of the ablated UO_2 for Th^{70+}. This value is significantly higher than for defect mediated sputtering. Two factors determine the secondary ion yield, the initial ionization density and the re-neutralization of ions during the emission process. The absence of significant amounts of multiply charged secondary ions points to relatively low ionization densities even in the center of the impact site [144]. A low ionization density (i.e. at average less than one removed electron per molecule) makes it questionable if conditions for Coulomb explosions can be achieved. Recent molecular dynamics simulations predict ionization probabilities similar to values reported here for Coulomb explosion sputtering of silicon [139,177]. However, reneutralization dynamics and initial ionization density can not be de-convoluted easily.

The energy distribution of sputtered ions is another signature of the sputtering process. TOF-peaks of U^+ show a significant broadening to shorter flight times, indicating a fraction of ions emitted with higher initial energies than U_2^+ and other cluster ions [10]. This being the case, most probable initial energies of atomic and molecular ions still appear to be similar and, contrary to predictions for Coulomb explosions [141], no strong effect of projectile charge on the initial energy of positive secondary ions has been observed so far. However, initial energies in reference [141] were calculated only for protons. Detailed simulations of initial energies of sputtered target ions and neutrals under realistic ionization conditions are clearly desirable.

Yet another signature of the sputtering process is the angular distribution of secondary ions and neutrals. To date, data are available only for low charge states up to 11+ [113] and no evidence for enhanced emission in foreword direction, which would be expected for Coulomb explosions [141,145], has been reported.

Investigating cluster emission from SiO_2 [127] and UO_2 [146], power law dependencies of cluster ion yields as a function of cluster sizes have been observed, consistent both with a Coulomb explosion-shock wave model [145] and a model considering a liquid–gas phase transition of an energized surface region [147].

The q-dependency of cluster ion emission (Fig. 16) indicates a qualitative change in the sputtering mechanism once the critical excitation strength is surpassed. It is important to note that a threshold charge, $q \approx 35+$, was also observed for the formation of blister like defects on mica surfaces [2,148,178]. Defect formation in this layered insulator was interpreted as resulting from electrostatic repulsion of positively charged layers after electrons have been emitted in the course of interaction with SHCI [148,149,178]. However, only a few percent of the total potential energy is dissipated through electron emission into the vacuum [149,150]. It must be viewed as a significant shortcoming of a pure Coulomb explosion concept to consider only target ionization and to ignore the effect of electronic excitations of target atoms.

4.3. Sputtering by intense, ultrafast electronic excitations

A third model considers the effect of high densities of electronic excitations on the structural stability of covalent solids (e.g., Si, GaAs and SiO_2) [151,179]. This model was originally developed to describe non-thermal phase transitions of semiconductors induced by intense ultrafast electronic excitations from femtosecond lasers.

Structural instabilities arise directly from destabilization of atomic bonds by high-density electronic excitations. Structural changes are induced in covalent solids when ~10% of valence electrons are promoted from bonding states in the valence band to anti-bonding states in the conduction band. Each electron-hole excitation causes a repulsive force between atoms. In GaAs, the resulting pressure is predicted to displace atoms by ~0.1 nm within only ~200 fs [151,179]. In contrast, heat exchange from excited electrons to the lattice requires many picoseconds. A critical laser fluence to induce such a phase transition in GaAs is ~0.8 kJ/m^2 [151,152,179] or ~5 keV/nm^2 where a characteristic absorption depth is ~1 μm [143]. Potential energies of SHCI used in the study of Schenkel et al. [30] range from 10.5 keV (Xe^{27+}), 51.3 keV (Xe^{44+}) and 67.8 keV (Th^{56+}) to 152.6 keV (Th^{70+}). When these energies are deposited into a solid by SHCI, the energy densities span and considerably exceed this value for the critical fluence. Recent molecular dynamics simulations of ultrashort pulse laser ablation of silicon have included effects of high-density electronic excitations [143]. Ablation rates per laser shot in a high fluence (~120 kJ/m^2), high energy density (~0.75 keV/nm^3) regime are ~400–1000, the same magnitude as observed for HCI like Th^{56+} and Th^{70+} interacting with GaAs. This comparison of predictions from a model of structural instabilities and sputter yield measurements can only be qualitative at this point. Clearly, more detailed simulations of ablation rates, secondary ion yields and the mass distribution of ablated particles as a function of excitation conditions are very desirable both for SHCI and femtosecond laser based excitations.

4.4. Microscopic mechanisms for sputtering by SHCI: conclusions

Currently available data on electronic sputtering by SHCI are summarized in Table 4. The third column indicates whether or not a charge state dependency of the total sputtering yield was observed. Results are most controversial for GaAs. While the defect mediated sputtering model does not apply [25,114], a decrease of the ionization probability with q is also inconsistent with the concept of sputtering through Coulomb explosions [139,141,153,177]. Very high sputtering yields are consistent with a mechanism of structural instabilities induced by ultra fast, intense electronic excitation [30]. However, only qualitative comparison with predictions from model calculations is possible so far [143].

If Coulomb explosions were possible, they should result in sputtering yield increases as a function of q for all insulators. Uranium oxide is the first material for which q-dependent sputter yields were measured and that is not known to form localized defects. Even so, it is still possible that some localized defects are formed in UO_2 and that their subsequent decay contributes to SHCI induced sputtering of mostly neutral uranium atoms. On the other hand, the increase of the ionization probability with q is clearly inconsistent with the notion of defect mediation as sole sputtering mechanism. Also, the observation of high yields of heavy cluster ions and the onset of cluster emission at a relatively high projectile charge (i.e. ~35+ for xenon) point towards Coulomb explosion sputtering. The fraction of secondary ions from uranium oxide is much higher than in defect-mediated sputtering, but it still comprises only a small part of ablated material. We suggest that structural instabilities also contribute to the ablation of the heavy metal oxide. Pure defect mediated sputtering is likely to dominate particle emission for alkali halides under conditions of relatively low excitation densities, i.e., for projectiles with charge states $<30+$. Here, the response of the solid can be described with well-known processes from a wealth of DIET studies [137,154]. The situation changes when projectiles with higher charge states are used. Our results indicate the onset of a qualitatively different behavior once q exceeds $\sim 35+$ and the available potential energy exceeds ~ 25 keV. Decay of individual defects will still play a role in the materials where such defects (such as STE and STH) can be localized, but the interaction of many defects ($\gg q$) in a small volume (tens of nm^3) of material causes a qualitatively new response of the excited solid. Clearly, de-convolution of contributions from Coulomb explosions, structural instabilities and decay of individual defects will have to be addressed in future studies.

5. Emerging applications

Singly charged ion beams are used in various applications in microelectronics, biotechnology, and photonics. Examples of the widely used techniques are ion implantation for local doping of electronic devices and secondary ion mass spectroscopy for surface and bulk analysis. Work in the area of emerging applications has concentrated on substituting SHCI beams for singly charged beams in conventional ion beam techniques.

5.1. Highly charged ion based secondary ion mass spectrometry

Secondary ion mass spectrometry (SIMS) describes a group of very powerful surface analytical techniques that have been in use for more than 30 years. The SIMS technique involves a primary ion beam of typically 0.5–30 keV energy impinging on a sample surface and then extracting the generated secondary ions. The secondary ions are separated according to their mass-to-charge ratio by electric or magnetic fields or by their flight time. The separated ions are detected by an ion multiplier. In conventional SIMS the primary ions are usually ionized Ar, Xe, Kr, O, Cs, or Ga atoms. There are two types of SIMS techniques, ‘dynamic’ or ‘static’. In dynamic mode the primary ion current is high and the sample is quickly eroded and elemental concentration of the bulk material is measured. Almost all surface and molecular information is lost. In static mode the primary ion current is low with doses less than 1×10^{12} ions/cm^2. The great advantage of static SIMS that makes this technique so popular is its extreme surface sensitivity in the parts per million range (i.e. about 10^9 atoms/cm^2 can be detected).

Conventional, static, singly charged ion SIMS is in general not a quantitative technique for measuring surface concentrations. The reason for the non-quantitative nature of SIMS is the unknown ion production probability as a function of the chemical environment of the surface. This problem is most often solved by the use of calibration standards. Schenkel et al. [126] have investigated the use of highly charged ions as the primary source to make SIMS quantitative without the use of calibration standards. The intense perturbation of the electronic system of the surface by SHCI enhances the ionization probability of the moieties leaving the surface, improving the quantification of SIMS. The system chosen for study was heavily boron-doped SiO_2 films. This case might be considered favorable to both conventional SIMS and SHCI based SIMS since the ionization potentials for B (8.23 eV) and Si (8.15 eV) are quite close. For an O^- primary ion beam conventional SIMS underestimated the true concentration as determined by *elastic recoil detection* (ERD) by a factor of 2.5, whereas the HCI-SIMS measured the true concentration to within 10% (the experimental error of the ERD). For less favorable cases such as O (I.P. 13.6 eV) stoichiometry of the silicon oxide, conventional SIMS underestimates the oxygen concentration by orders of magnitude, whereas, SHCI-SIMS also underestimates the oxygen concentration, but only by a factor of 2.5. The strong de-coupling of the ion production probability from the elemental ionization potential afforded by HCI enables a more quantitative analysis of surface layers.

The unusual surface phenomena that occur in SHCI-surface interactions have been recently applied to protein and DNA fragmentation [130]. The TOF-SIMS with SHCI of proteins and amino acids shows the desorption of intact molecules as well as fragmentation of the molecules into a number of fragments. Again the

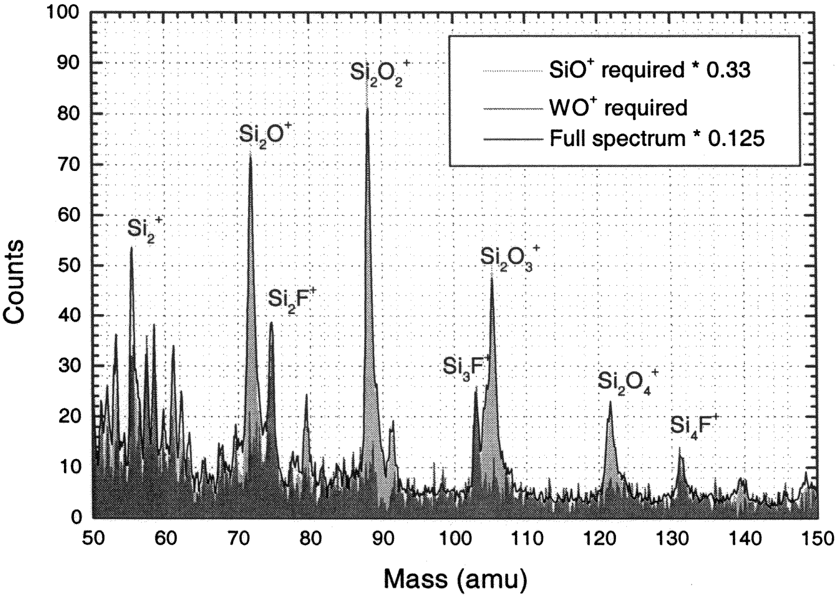

Fig. 18. Coincidence counting time-of-flight positive secondary ion mass spectrum from a $W/SiO_2/Si$ test wafer with a Th^{75+} primary beam ($E_{kin} = 262.5$ keV). The black line is the full spectrum; the SiO^+ coincidence spectrum is shown in light gray and the WO^+ coincidence spectrum is shown in gray. The spectra are scaled based on the relative number of sweeps used to build each spectrum [155].

secondary ion yield for these biomaterials were shown to increase with the charge state of the incident ion. In addition, irradiation of plasmid DNA with SHCI resulted in dramatic morphology changes observed by atomic force microscopy.

5.1.1. Coincidence counting

Nanoscopic information on the chemical heterogeneity of a surface can be obtained via coincidence counting techniques in slow, highly charged ion based SIMS. As the analyzed area shrinks to tens of nanometers the number of surface atoms becomes so small that detection of constituents becomes next to impossible. Coincidence counting allows many similar features to be interrogated simultaneously. The requirements for coincidence counting are that the secondary ion yield be high so that more than one secondary ion may be detected per primary ion event and that each primary event may probe a small, nanoscopic, area of the surface.

The interaction of SHCI with surfaces results in the emission of a large number of secondary ions per primary ion which increases with the charge of the incident ion [2,10,19,33]. For example, Au^{69+} impinging on 50 nm thick SiO_2 layer on a Si wafer induces a positive secondary ion yield per primary ion of 20. The surface area addressed by each highly charged ion can be estimated from the size of blisters observed for single ion impacts on mica surfaces [148,178]. The diameter of the blisters increases from 10 to 40 nm with incident charge from 35+ to 70+. Thus, SHCI excitation is very well suited to coincidence TOF-SIMS.

Hamza et al. [155] have demonstrated the utility of coincidence counting in TOF-SHCI-SIMS for impurity detection on patterned tungsten/SiO_2/Si wafers. Fig. 18 shows a portion of the positive TOF secondary ion mass spectrum for a Th^{75+} primary beam with 262.5 keV kinetic energy. Summing all of the collected events gives the spectrum labeled ‘full spectrum’. Coincidence mass spectra selecting only events which have the secondary ion SiO^+ or WO^+, respectively, are also shown. The most probably observed tungsten features were WO_x^+ secondary ions. The Si_2O_x series is highly correlated to the SiO^+ secondary ion and the Si_xF series is highly correlated to the WO^+ secondary ion. The coincidence counting technique shows that the Si_xF impurity is localized on the deposited tungsten regions and can be assigned as a result of the WF_6 reduction step in processing.

In this example, the tungsten features are rather large (greater than or equal to a micron) and other techniques could have been applied to determine the location of the Si_xF impurity, i.e., focused ion beam secondary ion mass spectroscopy or scanning Auger electron microscopy. However, as the feature sizes get smaller the number of impurity atoms or molecules analyzed in the focus area of the ion beam becomes vanishing small. The coincidence technique can analyze many similar features simultaneously, thus, removing the restrictions due the number of impurities in one small feature. In addition, the highly charged ion primary beam gives a higher ionization probability [10] and hence a higher useful yield, particularly for molecular species, for sensitive analysis of small features.

5.2. Emission microscopy

Barnes et al. [156] reported on a new emission microscopy technique with the potential to offer both high spatial resolution and very sensitive compositional analysis. This first instrument was designed and built to demonstrate the concepts necessary to construct a higher resolution instrument. The emission microscopy uses SHCI as the excitation source. The SHCI source brings four crucial advantages, a large secondary electron yield, high secondary ion yields, high ionization probability of the secondary emission, and high molecular ion yields. The objective (immersion) lens accelerates the secondary electrons and ions through the flight tube to a position sensitive detector. TOF is used to determine the mass-to-charge ratio of the secondary ions. This new instrument is unique in that it can combine high surface sensitivity (10^{10} atoms/cm^2) with high spatial resolution (in principle 100 nm) and chemical structure information (due to the high molecular ion yields). An example of a SHCI-emission microscope image is shown in Fig. 19.

5.3. SHCI driven X-ray source

Due to the high conversion efficiency of excitation energy into photons, several application schemes have been suggested in the literature. Here, the radiative de-excitation of focused SHCI beams provides the X-ray source via the interaction with a high transmission surface-target. An X-ray microscope [157] has been suggested and a prototype has been tested. SHCI are an extremely efficient source of X-rays, with a radiation yield on the order of 5% of the total energy, depending on the ion species and initial kinetic energy. The sample to be imaged is placed on or very close to the X-ray emitting surface, and the field of view is illuminated with SHCI impacts. X-rays transmitted through the sample are

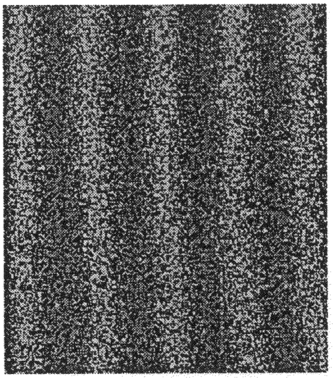

Fig. 19. Highly charged ion emission microscope image of 5 micron copper lines in SiO_2. The copper line spacing is 15 microns center to center. Lighter gray corresponds to the higher pulse height events, hence higher electron emission. Events are filtered also based on the secondary ion time-of-flight.

counted in a (non-imaging) X-ray detector. The position at which each detected X-ray entered the sample (i.e. the ion impact position) is determined by imaging the secondary electrons that are also emitted during highly-charged-ion recombination at the target surface. Each detected X-ray is 'tagged' with the two-dimensional position coordinates of the ion impact, and the tag provides the spatial information for the image. If a position sensitive X-ray detector, or multiple non-imaging detectors, are substituted for the single X-ray counter, then multiple views of the sample are acquired simultaneously. The techniques of tomography can then be used to reconstruct a fully three-dimensional image of the sample.

The extreme population inversion produced in these ion-surface interactions has the potential to be exploited for X-ray laser schemes if a highly-dense plasma could be produced against a metal surface. The multiphoton production of X-rays of wavelength 2–3 Å from highly ionized xenon atoms, which possess a large number of innershell vacancies, while retaining several electrons in relatively weakly bound outer orbitals, has been reported [158]. Atoms with this 'inverted' electronic configuration are designated 'hollow atoms'. We find that generation of hollow atoms can become the dominant excitation mode for such systems, making their exploitation in an X-ray laser a real possibility.

5.4. Surface modification

Controlled modifications of bulk and surfaces properties of materials by exposure to ion beams form a flourishing field of applied physics. Ion implantation is perhaps the most widely applied technique to develop from ion-solid interaction research. In this and other applications, the kinetic energy of the projectile is controlled to perform the desired materials modification. With recent advances in ion sources technology for highly charged ions (e.g., EBIT, EBIS, and ECR sources), it is now possible to explore surface modifications based on the potential energy the ions deposits into a near surface volume.

In an extension of their pioneering work, Rühlicke et al. [148] demonstrated with *atomic force microscopy* (AFM) the formation of blisters on mica surfaces upon single, highly charged ion impact. The volume of the blister was correlated with the charge of the incident ion, with a threshold for blister formation at a charge state of $q = 30$. Parks et al. [159] have repeated the measurements at constant kinetic energy (100 keV) of the incident Xe ions. They observed a similar blister volume dependence on the incident ion charge, again with a threshold at $\sim q = 30$. In addition Parks et al. [160] have confirmed the Rühlicke et al. [148,178] observation that the blister size is independent of the kinetic energy (20–800 keV) of the highly charged projectile.

The formation of single ion defects has also been observed on surfaces of other materials. Schenkel et al. [128] have measured single SHCI-induced defects on *self-assembled monolayers* (SAM) on silicon (111) wafers with atomic force microscopy. Xe^{41+} exposure of an octene SAM and Au^{63+} exposure of octene functionalized with CF_3-Phenol SAM produced craters of 50 ± 10 nm and $63 \pm$

14 nm diameter, respectively, as imaged in non-contact AFM mode (see Fig. 20). The tip radius was 70 nm, making crater depth measurement unreliable. However, secondary ion yields demonstrated that the entire SAM was removed, since Si ions from the substrate were observed. A damage cross section can be estimated from the crater diameter to be $\sim 2 \times 10^{-11}$ cm^2 for Xe^{41+} at 287 keV kinetic energy on the octene SAM.

Newman et al. [161] have measured the damage cross section for Xe^{44+} ions with 308 keV kinetic energy on fullerene films to be 6×10^{-12} cm^2. In the fullerene case, a combination of kinetic energy and a minor contribution from the potential energy deposition in the film leads to the observed damage cross section. This finding results from the relative robustness of fullerene cages to ionization and electronic excitation as compared to the more volatile SAMs on Si.

Single ion defects have also recently been observed in *polymethylmethacrylate* (PMMA) [162]. PMMA is a resist material used in lithography of semiconductor devices. Typically, the resist is exposed to ion, electron, or photon irradiation and then developed in a mixture of isopropyl alcohol and methyl isobutyl ketone. After development, Gillaspy et al. [162] found craters of ~25 nm diameter following the impact of single Xe^{44+} ions. Craters were not observed prior to resist development. When the integrated Xe^{44+} dose is increased to 2×10^{10} cm^{-2} and exposed through a nickel stencil mask, 1 μm dots can be observed on the PMMA substrate after developing. The feature morphology is consistent with the precision of the mask. The integrated dose necessary to fully expose the resist was approximately one order of magnitude lower than required for singly charged ions (i.e., Ga$^+$).

Suzuki and Itabashi [163] suggest that highly charged ions may be useful for advanced dry etching applications. Because the potential energy is deposited in the

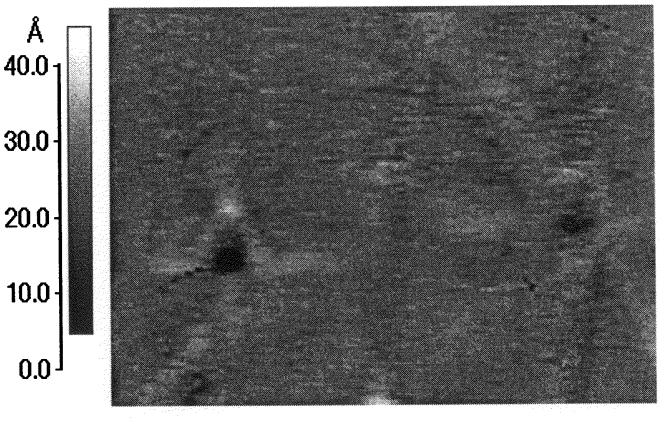

Fig. 20. Noncontact atomic force microscope image of an octene monolayer on Si(111) after exposure to Xe^{41+}. The average diameter of the impact craters is 50 ± 10 nm [128].

surface and the kinetic energy of the ions can be quite low, collateral damage may be eliminated.

Acknowledgements

This work was performed under the auspices of the US Department of Energy at Lawrence Livermore National Laboratory under contract number W-7405-ENG-48.

References

[1] A. Arnau, F. Aumayr, P.M. Echenique, M. Grether, W. Heiland, J. Limburg, R. Morgenstern, P. Roncin, S. Shippers, R. Schuch, N. Stolterfoht, P. Varga, T.J.M. Zouros, H.P. Winter, Surf. Sci. Rep. 27 (1997) 113.

[2] D.H.G. Schneider, M.A. Briere, Phys. Scr. 53 (1996) 228.

[3] J. Burgdörfer, P. Lerner, F.W. Meyer, Phys. Rev. A 44 (1991) 880.

[4] Z.Q. Xie, C.M. Lyneis, Rev. Sci. Inst. 66 (1995) 4218.

[5] Z.Q. Xie, Rev. Sci. Inst. 69 (1998) 625.

[6] G.D. Alton, F.W. Meyer, Y. Liu, J.R. Beene, D. Tucker, Rev. Sci. Inst. 69 (1998) 2305.

[7] T. Nakagawa, J. Ärje, Y. Miyazawa, M. Hemmi, T. Chiba, N. Inabe, M. Kase, T. Kageyama, O. Kamigaito, M. Kidera, A. Goto, Y. Yano, Rev. Sci. Inst. 69 (1998) 637.

[8] G. Shirkov, T. Nakagawa, Rev. Sci. Inst. 69 (1998) 1141.

[9] L.P. Ratliff, E.W. Bell, D.C. Parks, A.I. Pikin, J.D. Gillaspy, Rev. Sci. Inst. 68 (1997) 1998.

[10] T. Schenkel, A.V. Barnes, A.V. Hamza, J.C. Banks, B.L. Doyle, D.H. Schneider, Phys. Rev. Lett. 80 (1998) 4325.

[11] J.W. McDonald, D.H. Schneider, J.P. Briand, G. Machicoane, V. Leroux, in: EBIT Annual Report 96–97, Lawrence Livermore National Laboratory, UCRL-ID-132345 1999.

[12] M.P. Stöckli, M. Abdallah, C.Y. Chen, C.L. Cocke, B.D. De Paola, D. Fry, E. Gibson, P. Richard, T.N. Tipping, B. Walch, S. Winecki, B. Eastman, Th Gebel, E. Langer, U. Lehnert, H. Preusse, F. Ullmann, A. Georges, M. Ramassamy, Rev. Sci. Inst. 69 (1998) 665.

[13] M.P. Stöckli, Rev. Sci. Inst. 69 (1998) 649.

[14] A.V. Demyanov, S.V. Sidorov, S.A. Avdeev, B.P. Jatcenko, Rev. Sci. Inst. 69 (1998) 1156.

[15] M.A. Briere, T. Schenkel, D.H. Schneider, P. Bauer, A. Arnau, Phys. Scr. T73 (1997) 324.

[16] W. Huang, H. Lebius, R. Schuch, M. Grether, N. Stolterfoht, Phys. Rev. A 58 (1998) 2962.

[17] S. Winecki, C.L. Cocke, D. Fry, M.P. Stöckli, Phys. Rev. A 53 (1996) 4228.

[18] W. Huang, H. Lebius, R. Schuch, M. Grether, N. Stolterfoht, Phys. Rev. A 56 (1997) 3777.

[19] T. Schenkel, A.V. Barnes, M.A. Briere, A.V. Hamza, A. Schach von Wittenau, D.H. Schneider, Nucl. Inst. Meth. Phys. Res. B 125 (1997) 153.

[20] H. Eder, M. Vana, F. Aumayr, H.P. Winter, Rev. Sci. Inst. 68 (1997) 165.

[21] C. Lemell, J. Stöckl, J. Burgdörfer, G. Betz, H.P. Winter, F. Aumayr, Phys. Rev. Lett. 81 (1998) 1965.

[22] F. Aumayr, H. Kurz, D. Schneider, M.A. Briere, J.W. McDonald, C.E. Cunningham, H.P. Winter, Phys. Rev. Lett. 71 (1993) 1943.

[23] H. Ibach (Ed.), Electron Spectroscopy for Surface Analysis, Springer-Verlag, Berlin, Germany, 1977.

[24] T. Neidhart, F. Pichler, F. Aumayr, H.P. Winter, M. Schmid, P. Varga, Phys. Rev. Lett. 74 (1995) 5280.

[25] M. Sporn, G. Libiseller, T. Neidhart, M. Schmid, F. Aumayr, H.P. Winter, P. Varga, Phys. Rev. Lett. 79 (1997) 945.

[26] K.G. Liebbrecht, J.E. Griffith, R.A. Weller, T.A. Tombrello, Rad. Eff. 49 (1980) 195.
[27] J.C. Banks, B.L. Doyle, J.A. Knapp, D. Werho, R.B. Gregory, M. Anthony, T.Q. Hurd, A.C. Diebold, Nucl. Inst. Meth. Phys. Res. B. 138 (1998) 1223.
[28] A. Schnieders, R. Möllers, M. Terhorst, H-G. Cramer, E. Niehuis, A. Benninghoven, J. Vac. Sci. Tech. B 14 (1996) 2712.
[29] A.J. Chapman, Heat Transfer, Macmillan, New York, 1974.
[30] T. Schenkel, A.V. Barnes, A.V. Hamza, J.C. Banks, B.L. Doyle, D.H. Schneider, Phys. Rev. Lett. 81 (1998) 2590.
[31] A. Benninghoven, Surf. Sci. 299/300 (1994) 246.
[32] C.R. Brundle, C.A. Evans, S. Wilson, Encyclopedia of Materials Characterization, Butterworth-Heinemann, Stoneham, 1992.
[33] T. Schenkel, Zur Wechselwirkung langsamer hochgeladener Ionen mit Festkörpern, dissertation, Goethe Universität Frankfurt, April 1997 (unpublished).
[34] T. Schenkel, A.V. Hamza, A.V. Barnes, M.W. Newman, G. Machicoane, T. Niedermayr, M. Hattass, J.W. McDonald, K.J. Wu, R.W. Odom, D.H. Schneider, Proceedings of the IXth International Conference on the Physics of Highly Charged Ions, Bensheim, September 1998; Physica Scripta, in press.
[35] E. Steinbauer, P. Bauer, M. Geretschlager, G. Bortels, J.P. Biersack, P. Burger, Nucl. Inst. Meth. Phys. Res. B 85 (1994) 642.
[36] J-P. Briand, B. d'Etat, D. Schneider, M. Clark, V. Decaux, Nucl. Inst. Meth. Phys. Res. A 87 (1994) 138.
[37] M. LeGros, E. Silver, D. Schneider, J. McDonald, S. Bardin, R. Schuch, N. Madden, J. Beeman, Nucl. Inst. Meth. Phys. Res. A 357 (1995) 110.
[38] N. Bohr, Kgl. Danske Videnskab. Selskab. Mat.-fys. Medd. 18 (8) (1948).
[39] T. Schenkel, M.A. Briere, H. Schmidt-Böcking, K. Bethge, D. Schneider, Phys. Rev. Lett. 78 (1997) 2481.
[40] M. Grether, D. Niemann, A. Spieler, N. Stolterfoht, Phys. Rev. A 56 (1997) 3794.
[41] M. Hattass, T. Schenkel, A.V. Hamza, A.V. Barnes, M.W. Newman, J.W. McDonald, T.R. Niedermayr, G.A. Machicoane, D.H. Schneider, Phys. Rev. Lett., in press.
[42] W. Bambynek, et al., Rev. Mod. Phys. 44 (1972) 716.
[43] T.J. Grey, C.L. Cocke, R.K. Gardner, Phys. Rev. A 16 (1977) 190 and references therein.
[44] R. Loew, Nucl. Instr. Meth. 117 (1974) 505.
[45] B. Rosner, S. Datz, W. Wu, N.L. Jones, D.R. Schulz, C.O. Reinhold, Phys. Rev. A 57 (1998) 2737.
[46] W. Brandt, R. Laubert, M. Mourino, A. Schwartzchild, Phys. Rev. Lett. 30 (1973) 358.
[47] D. Pines, in: F. Seitz, D. Turnbull (Eds.), Solid State Physics, vol. 1, Academic, New York, 1955.
[48] U. Falke, Fresius J. Anal. Chem. 349 (1994) 241.
[49] K.R. Karim, S.R. Grabe, C.P. Bhalla, J. Phys. B 29 (1996) 4007.
[50] J.P. Briand, B. d'Etat-Ban, D. Schneider, M.A. Briere, V. Decaux, J.W. McDonald, S. Bardin, Phys. Rev. A 53 (1996) 2194.
[51] S. Winecki, M.P. Stöckli, C.L. Cocke, Phys. Rev. A 56 (1997) 538.
[52] W. Huang, H. Lebius, R. Schuch, M. Grether, A. Spieler, N. Stolterfoht, Nucl. Inst. Meth. Phys. Res. B 135 (1998) 336.
[53] F.W. Meyer, O. Yan, P. Zeijlmans van Emmichovan, I.G. Hughes, G. Spierings, Nucl. Inst. Meth. Phys. Res. B 125 (1997) 138.
[54] O.B. Firsov, Sov. Phys. JETP 36 (1959) 1076.
[55] J. Lindhard, M. Scharff, Phys. Rev. 124 (1961) 128.
[56] J. Knipp, E. Teller, Phys. Rev. 59 (1941) 659.
[57] P. Sigmund, Phys. Rev. A 50 (1994) 3197.
[58] J.P. Biersack, Nucl. Inst. Meth. Phys. Res. B 80/81 (1993) 12.
[59] W.N. Lennard, T.E. Jackman, D. Phillips, Phys. Lett. A 79 (1980) 309.
[60] T. Schenkel, M.A. Briere, A.V. Barnes, A.V. Hamza, K. Bethge, H. Schmidt-Böcking, D. Schneider, Phys. Rev. Lett. 79 (1997) 2030.

[61] R. Herrmann, C.L. Cocke, J. Ullrich, S. Hagmann, M. Stoeckli, H. Schmidt-Böcking, Phys. Rev. A 50 (1994) 1435.

[62] J.I. Juaristi, A. Arnau, Nucl. Inst. Meth. Phys. Res. B 115 (1996) 173.

[63] A. Arnau, M. Peñalba, P.M. Echenique, F. Flores, Nucl. Inst. Meth. Phys. Res. B 69 (1992) 102.

[64] H. Khemliche, J. Limburg, R. Hoekstra, R. Morgenstern, N. Hatke, E. Luderer, W. Heiland, Nucl. Inst. Meth. Phys. Res. B 125 (1997) 116.

[65] A. Arnau, Nucl. Inst. Meth. Phys. Res. B 115 (1996) 2.

[66] S. Winecki, M.P. Stöckli, C.L. Cocke, Phys. Rev. A 55 (1997) 4310.

[67] J.I. Juaristi, A. Arnau, P.M. Echenique, C. Auth, H. Winter, Phys. Rev. Lett. 82 (1999) 1048.

[68] H. Khemliche, T. Schlathölter, R. Hoekstra, R. Morgenstern, S. Shippers, Phys. Rev. Lett. 81 (1998) 1219.

[69] D. Niemann, M. Grether, M. Rösler, N. Stolterfoht, Phys. Rev. Lett. 80 (1998) 3328.

[70] R.A. Baragiola, C.A. Dukes, Phys. Rev. Lett. 76 (1996) 2547.

[71] Muino R. Diez, N. Stolterfoht, A. Arnau, A. Salin, P.M. Echenique, Phys. Rev. Lett. 76 (1996) 4636.

[72] Muino R. Diez, A. Salin, N. Stolterfoht, A. Arnau, P.M. Echenique, Phys. Rev. A 57 (1998) 1126.

[73] A. Arnau, Phys. Scr. T73 (1997) 303.

[74] D. Niemann, M. Grether, A. Spieler, N. Stolterfoht, C. Lemell, F. Aumayr, H.P. Winter, Phys. Rev. A 56 (1997) 4774.

[75] D. Niemann, M. Rösler, M. Grether, N. Stolterfoht, Nucl. Inst. Meth. Phys. Res. B 135 (1998) 460.

[76] J. Ducree, J. Mrogenda, E. Reckels, M. Rüther, A. Heinen, Ch Vitt, M. Venier, J. Leuker, H.J. Andrä, Muino R. Diez, Phys. Rev. A 57 (1998) 1925.

[77] J. Ducree, J. Mrogenda, E. Reckels, M. Rüther, A. Heinen, Ch Vitt, M. Venier, J. Leuker, H.J. Andrä, Phys. Rev. A 58 (1998) R1649.

[78] J. Thomaschewski, J. Bleck-Neuhaus, M. Grether, A. Spieler, D. Niemann, N. Stohlterfoht, Nucl. Inst. Meth. Phys. Res. B 125 (1997) 163.

[79] J. Thomaschewski, J. Bleck-Neuhaus, M. Grether, A. Spieler, N. Stohlterfoht, Phys. Rev. A 57 (1998) 3665.

[80] V.A. Morosov, M.N. Gaboriaud, M. Barat, P. Roncin, Nucl. Meth. Phys. Res. B 125 (1997) 167.

[81] L. Hägg, C.O. Reinhold, J. Burgdörfer, Phys. Rev. A 55 (1997) 2097.

[82] J.J. Ducree, F. Casali, U. Thumm, Phys. Rev. A 57 (1998) 338.

[83] Q. Yan, F.W. Meyer, in: Proceedings of the 13th International Conference on Defects in Insulating Materials—ICDIM 96, 1997. 239. p. 629.

[84] T. Niedermayr, A.V. Hamza, A.V. Barnes, T. Schenkel, M.W. Newman, J.W. McDonald, G. Machicoane, M. Hattass, (submitted for publication).

[85] N. Stolterfoht, D. Niemann, M. Grether, A. Spieler, A. Arnau, C. Lemell, F. Aumayr, H.P. Winter, Nucl. Inst. Meth. Phys. Res. B 124 (1997) 303.

[86] C. Lemell, H.P. Winter, F. Aumayr, Nucl. Inst. Meth. Phys. Res. B 125 (1997) 146.

[87] H. Winter, C. Auth, R. Schuch, E. Beene, Phys. Rev. Lett. 71 (1993) 1939.

[88] L. Folkerts, R. Morgenstern, in: E. Salzborn, P.H. Mokler, A. Müller (Eds.), Atomic Physics of Highly Charged Ions, 21, Z. Phys. D, Springer, Berlin, 1991, p. S351.

[89] E.D. Donets, Nucl. Inst. Meth. Phys. Res. B 9 (1985) 522.

[90] J.-P. Briand, J.P. Mosse, P. Indelicato, P. Chevallier, D. Girardvernhet, A. Chetioui, M.T. Ramos, J.-P. Desclaux, Phys. Rev. A 28 (1983) 1413.

[91] J-P. Briand, L. de Billy, P. Charles, S. Essabaa, P. Briand, R. Geller, J-P. Desclaus, S. Bliman, C. Ristori, Phys. Rev. Lett. 65 (1990) 159.

[92] J-P. Briand, S. Thuriez, G. Giardino, G. Borsoni, M. Froment, M. Eddrief, C. Sebenne, Phys. Rev. Lett. 77 (1996) 1452.

[93] B. d'Etat, J.-P. Briand, G. Ban, L. Debilly, J.-P. Desclaux, P. Briand, Phys. Rev. A 48 (1993) 1098.

[94] M.W. Clark, D. Schneider, D. Dewitt, J.W. McDonald, R. Bruch, U.I. Safranova, I.Y. Tolstikhina, R. Schuch, Phys. Rev. A 47 (1993) 3983.

[95] R. Schuch, D. Schneider, D.A. Knapp, D. DeWitt, J. McDonald, M.H. Chen, M. Clark, R.E. Marrs, Phys. Rev. Lett. 70 (1993) 1073.

[96] H.D. Hagstrum, Phys. Rev. 96 (1954) 325.

[97] J.P. Briand et al., private communication and APS March 99 meeting, Atlanta, USA.

[98] J.P. Mosse, P. Chevallier, J.P. Briand, Z. Phys. A 322 (1985) 207.

[99] N. Vaeck, J.E. Hansen, J. Phys. B 28 (1995) 3523.

[100] C.P. Bhalla, Phys. Rev. A 8 (1973) 2877.

[101] M. Chen, (personal communication).

[102] F.P. Larkins, J. Phys. B 9 (1971) L29.

[103] U.I. Safranova, I.Yn Tolstikhina, Phys. Scr. 47 (1993) 364.

[104] G. Omar, Y. Hahn, Phys. Rev. A 43 (1991) 4695.

[105] K.N. Huang, et al., Atomic Data Table 18 (1976) 243.

[106] D.A. Knapp, R.E. Marrs, M.B. Schneider, M.H. Chen, M.A. Levine, P. Lee, Phys. Rev. A 47 (1993) 2039.

[107] M.W. Clark, D. Schneider, E. Deveney, Q. Kessel, E. Pollack, W. Smith, Nucl. Inst. Meth. Phys. Res. B 79 (1993) 183.

[108] C. Froese-Fischer, Compt. Phys. Commun. 43 (1987) 355.

[109] H.J. Andrä, A. Simionovici, T. Lamy, A. Brenac, G. Lamboley, J.J. Bonnet, A. Fleury, M. Bonnefoy, M. Chassevent, S. Andriamonje, A. Pesnelle, in: Proceedings Fifth International Conference of the Physics of Highly Charged Ions, Giessen, September 1990. Z. Phys. D, 1990.

[110] S. Ninomiya, Y. Yamazaki, F. Koike, H. Masuda, T. Azuma, K. Komaki, K. Kuroki, M. Sekiguchi, Phys. Rev. Lett. 78 (1997) 4557.

[111] S. Ninomiya, Y. Yamazaki, T. Azuma, K. Komaki, K. Kuroki, Sekiguchi, Nucl. Inst. Meth. Phys. Res. B 135 (1998) 82.

[112] J.P. Briand, D. Schneider, S. Bardin, H. Khemliche, J. Jin, Z. Xie, M. Prior, Phys. Rev. A 55 (1997) 1.

[113] D.L. Weathers, T.A. Tombrello, M.H. Prior, R.G. Stokstad, R.E. Tribble, Nucl. Inst. Meth. Phys. Res. B 42 (1989) 307.

[114] P. Varga, T. Neidhard, M. Sporn, G. Libiseller, M. Schmid, F. Aumayr, H.P. Winter, Phys. Scr. T73 (1997) 307.

[115] K. Mochiji, N. Itabashi, S. Yamamoto, H. Shimizu, S. Ohtani, Y. Kato, H. Tanuma, K. Okuno, N. Kobayashi, Surf. Sci. 357 (358) (1996) 673.

[116] N. Itabashi, K. Mochiji, H. Shimizu, S. Ohtani, H. Tanuma, N. Kobayashi, J. J. Appl. Phys. Part 1 34 (1995) 6861.

[117] I.S. Bitenskii, E.S. Parilis, Atomnaya Energiya 46 (1978) 269.

[118] H.H. Andersen, A. Brunelle, S. Della-Negra, J. Depauw, D. Jacquet, Y. Le Beyec, J. Chaumont, H. Bernas, Phys. Rev. Lett. 80 (1998) 5433.

[119] S.T. de Zwart, T. Fried, D.O. Boerma, R. Hoekstra, A.G. Drentje, A.L. Boers, Surf. Sci. 177 (1986) L939.

[120] H. Gnaser, Low-Energy Ion Irradiation of Solid Surfaces, Springer, Berlin, 1999.

[121] N. Kakutani, T. Azuma, Y. Yamazaki, K. Komaki, K. Kuroki, J. J. Appl. Phys. 34 (1995) L580–L583.

[122] S. Della-Negra, J. Depauw, H. Joret, V. Le Beyec, E.A. Schweikert, Phys. Rev. Lett. 60 (1988) 948.

[123] J. Burgdörfer, Y. Yamazaki, Phys. Rev. A 54 (1996) 4140.

[124] M. Terasawa, T. Sekioka, T. Mitamura, S. Winecki, M.P. Stöckli, C.L. Cocke, Phys. Scr. T73 (1997) 326.

[125] E.S. Parilis, Z. Phys. D 21 (1991) S127 and references therein.

[126] T. Schenkel, A.V. Hamza, A.V. Barnes, D.H. Schneider, D.S. Walsh, B.L. Doyle, J. Vac. Sci. Tech. A 16 (1998) 1384.

[127] T. Schenkel, A.V. Barnes, A.V. Hamza, D.H. Schneider, Euro. Phys. J. D 1 (1998) 297.

[128] T. Schenkel, M. Schneider, M. Hattass, M.W. Newman, A.V. Barnes, A.V. Hamza, D.H. Schneider, J. Vac. Sci. Tech. B 16 (1998) 3298.
[129] T. Sekioka, M. Terasawa, T. Mitamura, M.P. Stöckli, U. Lehnert, C.L. Cocke, Nucl. Inst. Meth. Phys. Res. B 146 (1998) 172.
[130] C. Rühlicke, D. Schneider, M. Schneider, R.D. Dubois, R. Balhorn, Nanotechnology 9 (1998) 251.
[131] J.F. Ziegler, J.P. Biersack, U. Littmark, The Stopping and Range of Ions in Solids, Pergamon Press, New York, 1985.
[132] Z. Šroubeck, H. Oechsner, Surf. Sci. 348 (1996) 100.
[133] P. Sigmund, in: N.H. Tolk, J.C. Tully, W. Heiland, C.W. White (Eds.), Inelastic Ion-Surface Collisions, Academic Press, New York, 1977, p. 128.
[134] H.L. Bay, H.H. Anderson, W.O. Hofer, O. Nielsen, Nucl. Inst. Meth. Phys. Res. 132 (1976) 301.
[135] T. Schenkel et al., (to be published).
[136] F. Aumayr, J. Burgdörfer, P. Varga, H.P. Winter, Comm. At. Mol. Phys. 34 (1999) 201.
[137] N. Itoh, Nucl. Inst. Meth. Phys. Res. B 122 (1997) 405.
[138] O. Pankratov, M. Scheffler, Phys. Rev. Lett. 75 (1995) 701.
[139] H.P. Cheng, J.D. Gillaspy, Phys. Rev. B 55 (1997) 2628.
[140] R.L. Fleischer, P.B. Price, R.M. Walker, Nuclear Tracks in Solids, UC Press, Berkeley, 1975.
[141] I.S. Bitensky, E. Parilis, S. Della-Negra, Y. Le Beyee, Nucl. Inst. Meth. Phys. Res. B 72 (1992) 380.
[142] I.S. Bitensky, M.N. Murakhmetov, E.S. Parilis, Sov. Phys. Tech. Phys. 24 (1979) 618.
[143] R.F.W. Herrmann, J. Gerlach, E.E.B. Campbell, Appl. Phys. A 66 (1998) 35.
[144] G. Schiwietz, private communication.
[145] I.S. Bitensky, E.S. Parilis, Nucl. Inst. Meth. Phys. Res. B 21 (1987) 26.
[146] A.V. Hamza, T. Schenkel, A.V. Barnes, Eur. Phys. J. D. 6 (1999) 83.
[147] H.M. Urbassek, Nucl. Inst. Meth. Phys. Res. B 31 (1987) 541.
[148] C. Rühlicke, M.A. Briere, D. Schneider, Nucl. Inst. Meth. Phys. Res. B 99 (1995) 528.
[149] E. Parilis, Nucl. Instr. Meth. B 116 (1996) 478.
[150] J.W. McDonald, D. Schneider, M.W. Clark, D. Dewitt, Phys. Rev. Lett. 68 (1992) 2297.
[151] P. Stampfli, Nucl. Inst. Meth. Phys. Res. B 107 (1996) 138.
[152] L. Huang, J.P. Callan, E.N. Glezer, E. Mazur, Phys. Rev. Lett. 80 (1998) 185.
[153] Y. Yamamura, S.T. Nakagawa, H. Tawara, Nucl. Inst. Meth. Phys. Res. B 98 (1995) 400.
[154] T.E. Madey, Surf. Sci. 300 (1994) 824.
[155] A.V. Hamza, T. Schenkel, A.V. Barnes, D.H. Schneider, J. Vac. Sci. Tech. A 17 (1999) 303.
[156] A.V. Barnes, E. Magee, A.V. Hamza, T. Schenkel, D.H. Schneider, to be published.
[157] R.E. Marrs, D.H. Schneider, J.W. McDonald, Rev. Sci. Inst. 69 (1998) 204.
[158] A. McPherson, B.D. Thompson, A.B. Borisov, K. Boyler, C.K. Rhodes, Nature 370 (1994) 631.
[159] D.C. Parks, M.P. Stöckli, E.W. Bell, L.P. Ratliff, R.W. Schnieder, F.G. Serpa, J.D. Gillaspy, Nucl. Inst. Meth. Phys. Res. B 134 (1998) 46.
[160] D.C. Parks, R. Bastasz, R.W. Schmeider, M.P. Stöckli, J. Vac. Sci. Tech. B 13 (1995) 941.
[161] M.W. Newman, A.V. Hamza, T. Schenkel, A.V. Barnes, A. Machicoane, M. Hattass, T. Neidermayr, J.W. McDonald, to be published.
[162] J.D. Gillaspy, D.C. Parks, L.P. Ratliff, J. Vac. Sci. Tech. B 16 (1998) 3294.
[163] K. Suzuki, N. Itabashi, Pure Appl. Chem. 68 (1996) 1011.
[164] T. Schenkel, M.A. Briere, H. Schmidt-Böcking, K. Bethge, D. Schneider, Mat. Sci. Forum 248–249 (1997) 413.
[165] T. Neidhart, F. Pichler, F. Aumayr, H.P. Winter, M. Schmid, P. Varga, Nucl. Inst. Meth. Phys. Res. B 98 (1996) 465.
[166] F.F. Komarov, M.A. Kumakhov, Phys. Stat. Sol. B 58 (1973) 389.
[167] T. Schenkel, A.V. Hamza, A.V. Barnes, D.H. Schneider, Phys. Rev. A 56 (1997) R1701.
[168] A. Arnau, M. Peñalba, P.M. Echenique, F. Flores, Phys. Rev. Lett. 65 (1990) 1024.
[169] J-P. Briand, L. de Billy, P. Charles, S. Essabaa, P. Briand, R. Geller, J-P. Desclaux, S. Bliman, C. Ristori, Phys. Rev. A 43 (1991) 565.

[170] F. Aumayr, H.P. Winter, J. Limburg, R. Hoekstra, R. Morgenstern, Phys. Rev. Lett. 79 (1997) 2590.
[171] J.P. Briand, S. Thuriez, G. Giardino, G. Borsoni, M. Froment, M. Eddrief, C. Sebenne, Phys. Rev. Lett. 79 (1997) 2591.
[172] K. Mochiji, N. Itabashi, S. Yamamoto, H. Shimizu, S. Ohtani, Y. Kato, H. Tanuma, K. Okuno, N. Kobayashi, J. J. Appl. Phys. 34 (1995) 6861.
[173] N. Kakutani, T. Azuma, Y. Yamazaki, K. Komaki, K. Kuroki, Nucl. Inst. Meth. Phys. Res. B 96 (1995) 541.
[174] P. Sigmund, Appl. Phys. Lett. 25 (1974) 169.
[175] P. Sigmund, Appl. Phys. Lett. 27 (1975) 521.
[176] K. Baudin, A. Brunelle, S. Della-Negra, J. Depauw, Y. Le Beyec, in: G. Gillen, R. Lareau, J. Bennett, F. Stevie (Eds.), Secondary Ion Mass Spectrometry XI, Wiley, Chichester, 1998, p. 596.
[177] H.P. Cheng, J.D. Gillaspy, Comp. Mat. Sci. 9 (1998) 285.
[178] D. Schneider, M.A. Briere, M.W. Clark, J.W. McDonald, J. Biersack, W. Siekhaus, Surf. Sci. 294 (1993) 403.
[179] P. Stampfli, K.H. Bennemann, Appl. Phys. A 60 (1996) 191.